



# Particle acceleration in radio galaxies with flickering jets: GeV electrons to ultrahigh energy cosmic rays

James H. Matthews <sup>1</sup>★ and Andrew M. Taylor <sup>2</sup>

<sup>1</sup>*Institute of Astronomy, University of Cambridge, Madingley Road, Cambridge CB3 0HA, UK*

<sup>2</sup>*DES, D-15738 Zeuthen, Germany*

Accepted 2021 March 10. Received 2021 March 9; in original form 2020 December 11

## ABSTRACT

Variability is a general property of accretion discs and their associated jets. We introduce a semi-analytical model for particle acceleration and radio jet/lobe evolution and explore the effect of Myr time-scale jet variability on the particles accelerated by an active galactic nucleus (AGN) jet. Our work is motivated by the need for local powerful ultrahigh energy cosmic ray (UHECR) sources and evidence for variability in AGN and radio galaxies. Our main results are (i) UHECR and non-thermal radiative luminosities track the jet power but with a response set by the escape and cooling times, respectively; (ii) jet variability produces structure in the electron, synchrotron, and UHECR spectra that deviates from that produced for a constant jet power – in particular, spectral hardening features may be signatures of variability; (iii) the cutoff in the integrated cosmic ray (CR) spectrum is stretched out due to the variation in jet power (and, consequently, maximum CR energy). The resulting spectrum is the convolution of the jet power distribution and the source term. We derive an approximate form for a lognormal distribution of powers; and (iv) we introduce the idea of  $\sim 10$  GeV ‘proxy electrons’ that are cooling at the same rate that UHECRs of rigidity  $10$  EV are escaping from the source, and determine the corresponding photon frequencies that probe escaping UHECRs. Our results demonstrate the link between the history of an astrophysical particle accelerator and its particle contents, non-thermal emission, and UHECR spectrum, with consequences for observations of radio galaxies and UHECR source models.

**Key words:** acceleration of particles – magnetic fields – cosmic rays – galaxies: active – galaxies: jets – radiation mechanisms: non-thermal.

## 1 INTRODUCTION

Multiwavelength variability in the observed fluxes of accreting sources is observed on a range of time-scales. This flux variability has a number of near-universal characteristics. Often, the variability is consistent with ‘flicker’ noise, also known as  $1/f$  noise or pink noise because the power spectrum follows a  $1/f$  slope that is steeper than white noise but shallower than red. A pedagogical discussion of flicker noise in astronomy is given by Press (1978). A linear ‘rms–flux relation’ has been observed in X-ray binaries (Uttley & McHardy 2001; Uttley, McHardy & Vaughan 2005; Heil, Vaughan & Uttley 2012), accreting white dwarfs (Scaringi et al. 2012; Van de Sande, Scaringi & Knigge 2015), blazars (Biteau & Giebels 2012), and other X-ray active galactic nuclei (AGN; Uttley et al. 2005). A related phenomenon is a lognormal distribution of observed fluxes, seen in both disc-dominated (Gaskell 2004; Alston 2019) and jet-dominated sources (H. E. S. S. Collaboration 2010, 2017; Chevalier et al. 2019; see also Morris, Chakraborty & Cotter 2019). In addition to flickering-type variability, sources also undergo episodic bursts of accretion activity, with prominent examples being the outburst cycles of X-ray binaries (Fender, Belloni & Gallo 2004), restarting radio galaxies (Kaiser, Schoenmakers & Röttgering 2000; Brienza et al.

2018; Konar et al. 2019) and, possibly, the optical ‘changing-look’ phenomenon in quasars (LaMassa et al. 2015; MacLeod et al. 2016; Runnoe et al. 2016).

The accretion disc is intimately connected to the outflows produced by the system, which can take the form of winds or relativistic jets. If the jets are launched by the Blandford & Znajek (1977) mechanism, then for a black hole (BH) with gravitational radius  $r_g$ , the power of the jet depends on the BH spin parameter ( $a_*$ ) and magnetic flux ( $\Phi_B$ ) threading the event horizon as  $Q_{\text{BZ}} \propto c(a_* \Phi_B / r_g)^2$ . The precise relationship between the accretion rate,  $\dot{m}$ , and jet power is complicated; the production of powerful jets might require special conditions such as a magnetically arrested disc (MAD) state (Narayan, Igumenshchev & Abramowicz 2003; Tchekhovskoy, Narayan & McKinney 2011; Liska, Tchekhovskoy & Quataert 2018) and/or the presence of a disc wind to collimate the flow (e.g. Globus & Levinson 2016; Blandford, Meier & Readhead 2019). If we assume that  $\Phi_B^2$  is proportional to  $(\dot{m} c r_g^2)$  and that  $a_*$  changes on relatively long time-scales, then  $Q_{\text{BZ}} \propto \dot{m} c^2$ . This proportionality is also expected on general energetic grounds (e.g. Chatterjee et al. 2019; Davis & Tchekhovskoy 2020). It is therefore reasonable that the jet variability is in some sense a filtered version of the accretion-induced variability, a concept that has been successfully applied to jet modelling in X-ray binaries (Malzac 2014; Malzac et al. 2018). What effect does this jet variability have in AGN and radio galaxies? How do multiple episodes of accretion, which are themselves variable,

\* E-mail: [matthews@ast.cam.ac.uk](mailto:matthews@ast.cam.ac.uk)

affect the jet propagation, feedback, and any observable radiative or ultrahigh energy cosmic ray (UHECR) signatures?

In AGN, there are also long-term aspects of the accretion process that can imprint variability in the observed accretion flux and the power in the jet. For example, on long time-scales ( $\gtrsim$  Myr), the accretion rate is likely to be determined by the supply of cold gas to the central region of the galaxy. In the chaotic cold accretion model proposed by Gaspari (2016), the accretion rate on to the BH is predicted to follow a lognormal distribution with a pink/flicker noise power spectrum, just as is observed on shorter time-scales in accretion discs. Simulations by Yang & Reynolds (2016) also show flickering-type variability in the jet power caused by self-regulated accretion on to the central AGN, with jet power consequently varying over a large range, ( $>2$  dex; see also Beckmann et al. 2019). Long-term variability in jet power therefore seems inevitable from a fuelling perspective.

Astrophysical jets accelerate non-thermal particles (see Matthews, Bell & Blundell 2020 for a review), which radiate as they interact with magnetic fields or radiation. Our primary way of learning about radio galaxies is, as the name suggests, through radio emission from synchrotron-emitting electrons. As well as these non-thermal electrons, AGN jets can accelerate high-energy protons and ions, which we refer to as cosmic rays (CRs). The origin of the highest energy CRs, known as UHECRs, is not known. The maximum energy attainable in a particle accelerator is given by the Hillas energy  $E_H = Ze\beta BR$ , where  $\beta = u/c$  is the characteristic velocity,  $B$  is the magnetic field strength, and  $R$  is the size of the acceleration region. The Hillas energy is a general constraint that can be understood in terms of moving a particle of charge  $Ze$  a distance  $R$  through an optimally arranged  $-\mathbf{u} \times \mathbf{B}$  electric field. The Hillas criterion states that any accelerator must be a factor  $\beta^{-1}$  larger than the Larmor radius of the highest energy particles it accelerates, i.e.  $R > \beta^{-1} R_g(E_H)$ , where  $R_g$  denotes the Larmor radius. Calculating  $E_H$  with some characteristic numbers for radio galaxies reveals they are one of the few sources capable of reaching  $> \text{EeV}$  energies and accelerating UHECRs. For this reason, they have long been discussed as potential UHECR sources (e.g. Hillas 1984; Norman, Melrose & Achterberg 1995; Hardcastle et al. 2009; Eichmann et al. 2018; Matthews et al. 2018, 2019a), along with other classes of AGN jets and alternative sources such as gamma-ray bursts (GRBs), starburst winds, and cluster-scale shocks.

The Hillas energy can be used to obtain a power requirement for UHECR production, first derived using a dynamo model by Lovelace (1976), and discussed further by various authors (e.g. Waxman 1995; Blandford 2000; Eichmann et al. 2018; Nizamov & Pshirkov 2018). This power requirement is sometimes referred to as the Lovelace-Hillas or magnetic luminosity condition. If a particle reaches the Hillas limit, then the magnetic power must satisfy  $Q_B \gtrsim \beta^{-1} 10^{43} \text{ erg s}^{-1}$  for acceleration to a rigidity of  $E/Ze = 10 \text{ EV}$ . For reasonable departures from equipartition and accounting for a likely maximum energy some factor below  $E_H$ , UHECR acceleration probably requires kinetic jet powers in the region  $Q_j \gtrsim 10^{44} \text{ erg s}^{-1}$ . There are relatively few nearby radio galaxies (within the various UHECR horizons) capable of reaching these powers, if the current jet power estimates are taken at face value (Massaglia 2007b, a; Matthews et al. 2018, 2019a).

Any variability in the jet power will inevitably affect the morphology and dynamics of radio galaxies, as well as any feedback processes at work. There are now many examples of restarting or ‘double-double’ radio galaxies (e.g. Kaiser et al. 2000; Brienza et al. 2018; Konar et al. 2019), in which there appear to be distinct, discrete episodes of jet activity, but there is also subtler evidence for variability in the jet power. For example, Fornax A displays evidence

for a varied and complex history (Iyomoto et al. 1998; Lanz et al. 2010; Maccagni et al. 2020), while Centaurus A shows a distinction between different lobe structures on scales of  $\sim 2$  and  $\sim 300 \text{ kpc}$  (Morganti et al. 1999; Croston et al. 2009), which appear to be connected with different episodes of activity. The merger and gas fuelling history of the sources is complex in both Fornax A (e.g. Iyomoto et al. 1998; Mackie & Fabbiano 1998; Iodice et al. 2017) and Centaurus A (e.g. Stickel et al. 2004; Neff, Eilek & Owen 2015). In a more general sense, it is clear that there are many aspects of radio galaxies that are time integrated – for example, the total energy input into the surroundings, or the total energy stored in synchrotron-emitting electrons – and variability creates a disconnect between these integrated quantities and the instantaneous jet properties.

In this paper, our aims are threefold: (i) to introduce a numerical method capable of modelling, in a simple parametrized fashion, the morphology, radiation, and UHECR signatures from radio galaxies with variable jet power; (ii) to study the effect of jet variability on observational signatures such as the synchrotron luminosity and broad-band spectral energy distribution (SED); and (iii) to study the acceleration and escape of UHECRs in radio galaxies with variable jet powers. In our modelling, we focus on jets with a flicker noise power spectrum and a lognormal power distribution. We make a number of further simplifying assumptions and the model is unlikely to provide quantitative matches with real astrophysical sources. Indeed, our approach is mostly heuristic – we aim to demonstrate some key principles regarding particle acceleration in variable jets that can be used to study UHECR and electron acceleration. We begin by describing our method (Section 2) and present the results from a single simulation in Section 3. In Section 4, we introduce the concept of ‘proxy electrons’, before discussing extragalactic CR propagation, observational applications, and limitations of the model. We conclude in Section 5.

## 2 A SIMPLE VARIABLE JET AND PARTICLE INJECTION MODEL

We begin by introducing our model for the evolution of a flickering jet and the non-thermal particles it accelerates. The jet has a kinetic power that behaves stochastically according to an input power spectrum and probability density function (PDF); we begin by describing the process of generating this jet power time series, before describing the dynamics of the jet and the treatment of particle acceleration.

### 2.1 Synthetic jet power histories

To create a synthetic jet power time series, we use an input power spectral density (PSD) and jet power PDF to generate a time series for the jet power for a given set of PSD and PDF parameters. We use the method described by Emmanoulopoulos, McHardy & Papadakis (2013) and implemented in PYTHON by Connolly (2015). The algorithm is similar to the widely used Timmer & Koenig (1995) method, except that it allows for more flexibility in specifying the underlying. The PSD is specified as a power-law model of the form

$$\text{PSD}(f) \propto f^{-\alpha_p}, \quad (1)$$

where  $f$  is the temporal frequency. We set  $\alpha_p = 1$  for a ‘pink’ or flicker noise spectrum and use bins of  $0.1 \text{ Myr}$  when generating the synthetic time series. We use a lognormal distribution of jet power,  $Q_j$ , as our input PDF, given by

$$p(Q_j) = \frac{1}{Q_j \sigma \sqrt{2\pi}} \exp \left[ -\frac{(\ln Q_j / Q_0)^2}{2\sigma^2} \right], \quad (2)$$

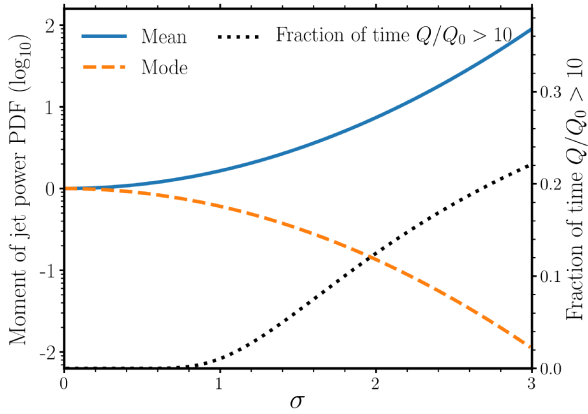


**Figure 1.** The relationship between various properties of a lognormal jet power distribution, plotted on a logarithmic (base 10) scale. The blue solid and orange dashed lines show the mean and mode of the distribution, given by  $e^{\ln Q_0 + \sigma^2/2}$  and  $e^{\ln Q_0 - \sigma^2}$ , respectively. The mean increases as  $\sigma$ , the natural logarithm of the standard deviation, increases. The black dotted line is shown on a different (linear) y-axis, and shows the fraction of time the jet has a power exceeding  $10Q_0$ . This is equivalent to the survival function of the distribution (or one minus the CDF) evaluated at  $10Q_0$ . The plot illustrates how a wider lognormal distribution (a more variable jet power) produces more favourable conditions for UHECR acceleration; as  $\sigma$  increases, the jet spends more time in a ‘high’ state and has a higher integrated energy output.

where  $\ln Q_0$  is the natural logarithm of the median jet power and  $\sigma$  is the standard deviation of  $\ln Q_0$ . The mean and mode of the distribution are given by  $\exp(\ln Q_0 + \sigma^2/2)$  and  $\exp(\ln Q_0 - \sigma^2)$ , respectively. These quantities are shown for comparison in Fig. 1.

As mentioned above, lognormal flux distributions are common in both disc- and jet-dominated accreting systems. In using a lognormal jet power distributions, we make an implicit assumption that some form of multiplicative process imprints variability on the jet on long time-scales. The mean of a lognormal distributions is larger than both the median and the mode. This asymmetry is important for UHECR production, since AGN jets must reach high powers ( $\gtrsim 10^{44}$  erg s $^{-1}$ ) in order to accelerate CRs to energies beyond 10 EeV. Furthermore, the jets that have higher values of  $\sigma$  (more variable) also have a greater difference between the mean and median values of  $Q$ .

We model the propagation of a jet with a constant mass density,  $\rho_j$ . The mass density is parametrized via a density contrast with the surrounding medium,  $\eta$ , which is defined as the density relative to density of the ambient medium at a radius of  $r = 0.1$  kpc. The jet nozzle has a constant radius,  $r_j$ . We assume that the power of the jet is variable and driven by accretion rate fluctuations, and that the jet is kinetically dominated (negligible jet pressure). The kinetic power of a one-sided relativistic jet can be derived from the equations of relativistic hydrodynamics (e.g. Taub 1948; Landau & Lifshitz 1975; Wykes et al. 2019) and is given by

$$Q_{j,1} = A_j v_j \Gamma_j (\Gamma_j - 1) \rho_j c^2, \quad (3)$$

where  $\rho_j$  is the jet mass density,  $\Gamma_j$  is the bulk Lorentz factor,  $A_j = \pi r_j^2$  is the cross-sectional area of the jet nozzle, and  $v_j$  is the jet velocity. We assume that the jet variability is entirely accounted for by variation of the jet velocity/Lorentz factor; thus, for a given value of the two-sided jet power  $Q_j = 2Q_{j,1}$ , we invert the above equation to solve for  $v_j$  (or equivalently,  $\Gamma_j$ ). The jet is transrelativistic, so the velocity is allowed to transition between non-relativistic and relativistic regimes. The jet power ultimately determines the jet advance speed, the energy input into the lobes, the

maximum CR energy, and the normalization of the particle source term (see subsequent sections). The mass input rate from the jet is  $\dot{M}_j = A_j v_j \Gamma_j \rho_j$ , which, together with the rate of change of volume, determines the density in the lobes.

## 2.2 Jet and lobe dynamics

A number of analytical and semi-analytical models for jet propagation have been developed (e.g. Begelman & Cioffi 1989; Falle 1991; Kaiser & Alexander 1997; Hardcastle 2018; Turner, Shabala & Krause 2018). Generally, these models concern themselves with relatively powerful jets that are well confined and Fanaroff–Riley type II (FR II)-like in their morphology; our approach is similar, with the main differences being that we allow for a flickering jet power and model the expansion of the lobe by discretizing into a series of cylindrical cells along the direction of propagation (the  $z$ -axis). We consider the propagation of a light jet, with typical density contrasts  $\sim 10^{-4}$ . The speed of the jet varies depending on the power, with typical Lorentz factors ranging from non-relativistic to  $\Gamma_j \approx 10$ . We assume that the advance of the jet is determined by equating, in the rest frame of the working surface, the momentum flux of the jet with that of the ambient medium (Marti et al. 1997), with an additional geometric factor (see Appendix A). We refer to the bubble inflated by the jet as a ‘lobe’ (rather than, say, a cocoon) throughout this paper for simplicity. The sideways expansion of the lobe is set by the bow-shock jump conditions, based on the difference in pressure between the lobe and surrounding environment. The lobe pressure is calculated in a self-consistent manner from the energy injection and volume of the lobe.

The jet propagates into an ambient medium with a density and pressure calculated from the ‘universal pressure profile’ described by Arnaud et al. (2010). This pressure profile is characterized by a single variable,  $M_{500}$ , which is the mass contained within the radius where the density is 500 times the critical density of the Universe. The ambient medium is assumed to be isothermal, with the temperature,  $T_c$ , set by the  $T_c$ – $M_{500}$  relation from Arnaud, Pointecouteau & Pratt (2005), which gives  $k_B T_c \approx 2.3$  keV for  $M_{500} = 10^{14} M_\odot$ . The density then follows from  $\rho = \mu m_p (P/k_B T)$ , where  $\mu = 0.62$  is the mean particle mass (we assume a fully ionized solar abundance plasma). This choice of parameters leads to a particle number density of  $n \approx 2 \times 10^{-3}$  cm $^{-3}$  at 100 kpc. The approximate functional dependence is a smooth broken power law of the form  $n(r) \propto (r/R_b)^{-\delta_1} [1 + (r/R_b)]^{(\delta_1 - \delta_2)}$ , with  $\delta_1 = 0.305$ ,  $\delta_2 = 5.70$ , and  $R_b = 715$  kpc for our adopted  $M_{500} = 10^{14} M_\odot$ . The domain is discretized in the direction of propagation,  $z$ , with  $N_z$  cells, and the evolution of the width of the lobe is calculated for each of the cells containing jet material. We compute a dynamic time-step and a particle evolution time-step, with the latter evolved during subcycles within the main dynamics loop. Our model for the jet dynamics is described further, with the relevant governing equations and more detail regarding the numerical scheme, in Appendix A. A schematic diagram describing the main features of the method is shown in Fig. 2.

## 2.3 Energy partitioning

To conduct our simulations, we have to decide what fraction of the jet’s kinetic power is transferred to the various forms of energy. Following Hardcastle (2018), we assume that a fraction  $\epsilon_w = 0.5$  of the jet’s power goes into doing PdV work on the surroundings (see also Blundell, Rawlings & Willott 1999; Bourne & Sijacki 2020); the remaining half is stored as internal energy in the lobes



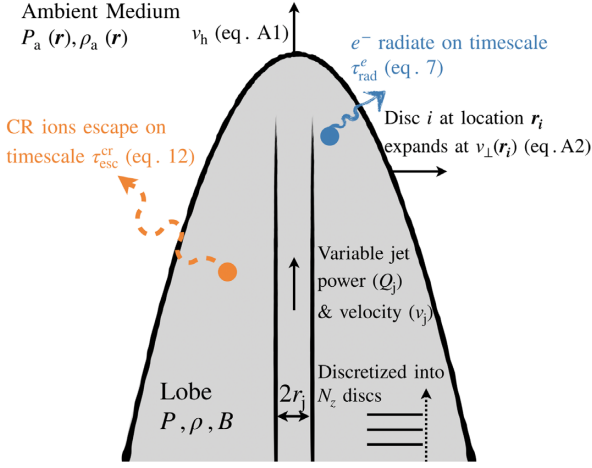


**Figure 2.** Schematically illustrating the main aspects of our method. A light, collimated jet propagates into an isothermal ambient medium with decreasing density and pressure, and inflates a cocoon or lobe. In the process it accelerates radiating electrons and CR ions, which gradually cool, and, in the case of CR ions, escape from the lobe. The dynamic model is described in Section 2.2 and Appendix A. The evolution of non-thermal particles is described in Section 2.4, and the escape of CR ions is described in Section 2.5.

and used to calculate the lobe pressure and sideways lobe expansion (see Appendix A). The use of this work factor is an approximation and while it is fairly accurate in estimating the overall  $PdV$  work done, it does not account for the fact that the work done varies over time and can in principle be higher than the energy input in periods of low jet power (see Appendix A for further details). The energetic particle populations comprise of non-thermal electrons ( $E_e$ ) and non-thermal protons and ions – which we refer to as CRs ( $E_c$ ). We assume that a fraction  $\epsilon_e$  of the jet power is transferred into non-thermal electrons, such that  $dE_e/dt = \epsilon_e Q_j$ . For simplicity, we assume the same amount of energy is transferred into CRs, giving  $dE_c/dt = \epsilon_c Q_j$  where  $\epsilon_c = \epsilon_e$ . The equations and source terms for the particle populations are given in Sections 2.4.2 and 2.4.1 and account for adiabatic losses. For the magnetic field, we set  $dE_B/dt = \epsilon_w \epsilon_b Q_j$ .

Our energy partitioning factors are defined at injection, so the fact that the different components cool at different rates means that these quantities differ to the instantaneous equipartition factors often used in the literature. In addition, our quantities are defined as a fraction of the total jet power rather than relative to other components. For the equation of state of lobe plasma, we use an adiabatic index of  $4/3$ , although a four-fluid ‘effective adiabatic index’ could be adopted, in a manner similar to Pfrommer et al. (2017). The partitioning factors adopted in our simulations are given in Table 1. We experimented and chose values that gave reasonable radio luminosities and typical magnetic field strengths in the lobe of tens of  $\mu\text{G}$ , in line with the results of Croston et al. (2004).

## 2.4 Non-thermal particles

AGN jets transfer energy to non-thermal particles. We model this process by evolving populations of both electrons and various CR ion species, with a source term that depends on the jet power. We do not model the particle acceleration physics, and we remain ambivalent about the details of the process. We assume that the particles are accelerated in e.g. shocks close to the jet head, over a short acceleration time,  $\tau_{\text{acc}} \sim \eta_g (r_g/c)$ , where  $\eta_g$  is the so-called gyrofactor (e.g. Aharonian 2000) such that  $\eta_g \approx 1$  in the Bohm

regime. We then allow the particles to cool in (and escape from) the lobe of the radio galaxy. Hereafter, we use the subscript  $e$  to denote electrons and  $i$  to denote CR ion species.

### 2.4.1 Non-thermal electrons

We evolve the electrons in the lobes according to the continuity equation

$$\frac{dn_e(E)}{dt} = \frac{d}{dE} \left( \frac{En_e(E)}{\tau_e(E)} \right) + S_e(E, t), \quad (4)$$

where  $n_e(E) = dN_e/dE$  is the differential spectrum of electrons at energy  $E$ . The first term accounts for synchrotron, inverse Compton (IC), and adiabatic losses through the total cooling time-scale  $\tau_e(E)$ , and  $S_e(E, t)$  is the electron source term, given by

$$S_e(E, t) = \frac{\epsilon_e Q_j(t)}{\chi_e} E^{-p} e^{-E/E_{\text{max},e}}, \quad (5)$$

where  $\chi_e$  is a normalization constant and  $\chi_e = \ln(E_{\text{max},e}/E_{0,e})$  for  $p = 2$ . The injection energy is set to  $E_{0,e} = 10m_e c^2$ . The maximum electron energy  $E_{\text{max},e}$  is kept constant at 100 TeV. We have verified that this maximum energy is achievable for the range of input jet powers, under the assumption that the maximum particle energy is limited by synchrotron cooling in the jet hotspot. However, the exact value is not well constrained. We discuss the reasons for this and possible improvements further in Section 4.5. We solve equation (4) following the method described by Chang & Cooper (1970) and Chiaberge & Ghisellini (1999), in which the equation is discretized and written in tridiagonal matrix form and then solved using a tridiagonal matrix algorithm (TDMA; also known as a Thomas algorithm). The total radiative cooling rate due to IC and synchrotron processes for electrons with energy  $E$  is

$$\left. \frac{dE}{dt} \right|_{\text{rad}} = \frac{E}{\tau_{\text{rad}}^e(E)}, \quad (6)$$

where

$$\tau_{\text{rad}}^e(E) = \frac{9}{4\alpha} \frac{U_{B,\text{crit}}}{U_B + U_{\text{rad}}} \frac{\hbar}{E}. \quad (7)$$

Here,  $U_B = B^2/8\pi$  is the magnetic field energy density,  $U_{\text{rad}}$  is the radiation field energy density, and  $U_{B,\text{crit}}$  is the energy density of the Schwinger field,  $B_{\text{crit}} = 4.41 \times 10^{13} \text{ G}$ . We set  $U_{\text{rad}} = 4.17 \times 10^{-13} \text{ erg cm}^{-3}$ , corresponding to the energy density of the cosmic microwave background (CMB) as reported by Fixsen (2009). The energy density of the CMB is equivalent to that of a  $3.24 \mu\text{G}$  magnetic field. We assume that the CMB is the dominant radiation field in our simulations, which is not true close to the host galaxy, but is likely to be a good approximation once the lobe has reached  $\sim 10 \text{ kpc}$  in length. Both electrons and CR ions also lose energy adiabatically as the lobe expands at the rate  $dE/dt|_{\text{ad}} = 1/3(E/V)dV/dt$ . The adiabatic loss time-scale is then  $\tau_{\text{ad}} = E/(dE/dt|_{\text{ad}})$ , and the total cooling time-scale is given by the reciprocal sum such that

$$\tau_e(E) = \left[ \frac{1}{\tau_{\text{ad}}} + \frac{1}{\tau_{\text{rad}}^e} \right]^{-1}. \quad (8)$$

### 2.4.2 Non-thermal ions (cosmic rays)

In the same manner as the electrons, we evolve a CR distribution for each CR ionic species,  $i$ , with a continuity equation that differs

**Table 1.** Main parameters used in the jet modelling, with definitions, value for the reference model, and references.

Parameter	Value	Description	Section/reference
$r_j$ (kpc)	0.5	Jet radius	–
$\epsilon_e$	0.15	Fraction of jet power that goes into non-thermal electrons	Section 2.3
$\epsilon_c$	0.15	Fraction of jet power that goes into CR ions	Section 2.3
$\epsilon_b$	0.1	Fraction of jet power that goes into magnetic field energy	Section 2.3
$\epsilon_w$	0.5	Fraction of jet energy that goes into doing $p dV$ work on the surroundings	Section 2.3
$f_i(Z_i, A_i)$	$f_\odot Z^2 A^{p-2}$	Injection fraction for ion $i$	Wykes et al. (2017)
$D_{\text{esc}}/D_B$	1	Escaping diffusion coefficient relative to Bohm	Section 2.5
$\eta_H$	0.3	Fraction of Hillas (1984) energy attainable	Section 2.4.2
$Q_0$ (erg s $^{-1}$ )	$10^{45}$	Median jet power	Section 2.1
$\sigma$	1.5	Jet variability parameter	Section 2.1
$p$	2	Injected particle spectral index	–
$\eta$	$10^{-4}$	Jet to ambient medium density contrast	–
$\rho_j$ (g cm $^{-3}$ )	$3.5 \times 10^{-30}$	Jet mass density	–
$M_{500}$ ( $M_\odot$ )	$10^{14}$	Ambient medium enclosed mass (sets pressure and density profile)	Arnaud et al. (2010)
$k_B T_c$ (keV)	2.3	Ambient medium temperature	Arnaud et al. (2005)
$\alpha_p$	1	Slope of temporal power spectrum	Section 2.1

slightly to the electrons, given by

$$\frac{dn_i(E)}{dt} = S(E/Z_i, f_i, t) - \frac{n_i(E)}{\tau_{\text{esc}}^{\text{cr}}(E/Z_i)} - \frac{n_i(E)}{\tau_{\text{loss}}(E, Z_i)} - \frac{n_i(E)}{\tau_{\text{ad}}}, \quad (9)$$

where  $n_i(E) = dN_i/dE$  is the differential spectrum of CR species  $i$  at energy  $E$ ,  $\tau_{\text{esc}}^{\text{cr}}$  is the CR escape time (see Section 2.5), and  $\tau_{\text{loss}}$  is the energy loss time-scale due to photoion, photodisintegration, and pair production losses. The total differential CR spectrum is then  $n(E, t) = \sum_i n_i(E, t)$ . We do not model the coupling between the different ion species (see below). We again use a power law with an exponential cutoff for the source term,  $S(E/Z_i, f_i, t)$ , given by (for  $p = 2$ )

$$S(E/Z_i, f_i, t) = \frac{f_i \epsilon_c Q_j(t)}{\chi_i} E^{-p} e^{-E/E_{\text{max},i}}, \quad (10)$$

where again  $\chi_i$  is a normalization constant and  $\chi_i = \ln(E_{\text{max},i}/E_0)$  for  $p = 2$ . The injection energy is assumed constant over time for each species and set to  $E_0 = 10 A_i m_p c^2$  (a CR Lorentz factor of 10). The maximum energy  $E_{\text{max}}$  at each time-step is set according to the power requirement for UHECR production based on the Hillas energy, which is discussed in the introduction, and is given by

$$E_{\text{max},i} = 10 \text{ EeV } Z_i \eta_H \left[ \frac{Q_j}{10^{44} \text{ erg s}^{-1}} \frac{\epsilon_b}{0.1} \beta_j \right]^{1/2}, \quad (11)$$

where  $\eta_H = E_{\text{max},i}/E_H$  denotes the fraction of the Hillas energy attainable. The maximum CR energy therefore accounts for the partitioning of magnetic energy via the term  $\epsilon_b$ . In addition, the use of this maximum energy condition ensures that the UHECR acceleration time is always short compared to  $r_j/c$ . It does also implicitly assume that particle acceleration is taking place close to the Bohm regime, but this must be the case for almost any UHECR accelerator (Hillas 1984). Our method could feasibly be made more complicated by incorporating more detailed aspects of shock acceleration physics. However, our approach here captures the general behaviour of the maximum CR energy depending on time through its dependence on the square root of the jet power, which has an important impact on the results.

The quantity  $f_i$  controls the relative fraction of ion  $i$  in the CR population. An enhancement of heavy ions relative to intrinsic abundance is expected on theoretical grounds (e.g. Ellison, Jones & Eichler 1981; Caprioli, Blasi & Amato 2011; Marcowith et al. 2016; Matthews et al. 2020), and there is empirical evidence for a heavy

composition in both Galactic CRs (e.g. Aglietta et al. 2004; Blasi & Amato 2012a) and UHECRs beyond the ankle (de Souza 2017; Pierre Auger Collaboration 2017). We take a phenomenological approach for charge and mass dependent injection that approximately fits the TeV-range Galactic CR spectrum, proposed by Wykes et al. (2017). In this approach, the spectrum in energy per nucleon is scaled by  $f_\odot Z^2/A$ , where  $A$  is the atomic mass number of the ion and  $f_\odot$  is the solar abundance. This is equivalent to setting  $f_i = f_\odot Z^2 A^{p-2}$ . We note that alternative scalings for chemical enhancements have been suggested, for example, by Caprioli, Yi & Spitkovsky (2017). However, the enhancement factor they propose is rather mild, scaling only as  $(A/Z)^2$ . We include all ions that are at least as abundant by number as Fe in the Sun (H, He, C, N, O, Ne, Mg, Si, and Fe).

For CR losses, we consider the normal loss mechanisms at ultrahigh energy ( $\gtrsim 1$  EeV), where protons undergo losses due to the GZK effect (Greisen 1966; Zatsepin & Kuz'min 1966), ions with  $A > 1$  undergo photodisintegration, and all species undergo pair production losses. For each of these processes, we tabulate rates from CRPROPA (Alves Batista et al. 2016) at  $z = 0$  for the CMB radiation field and the Gilmore et al. (2012) model for the extragalactic background light (EBL). We only include the CMB and EBL radiation fields and we do not allow for the cascade in decreasing  $A$  and  $Z$  for heavy nuclei as they photodisintegrate and lose nucleons; instead, we treat the process as an energy loss in equation (9) via the  $n_i/\tau_{\text{loss}}$  term. We do not include proton synchrotron losses in our model, because, although they can be important for  $10^{19}$  eV protons in  $\gtrsim 1$  mG fields (e.g. Aharonian 2002), the field strengths we consider instead range from 10 to 250  $\mu\text{G}$ , such that the proton synchrotron time-scale is longer than the simulation time even for the highest energy protons.

## 2.5 CR escape time

The escape time is difficult to estimate. Ultrahigh energy protons and ions will gradually escape out of the lobe via a combination of drifts, streaming, advection, and diffusion. We expect the particles to be accelerated in shocks relatively close to the jet head, although we remain ambivalent about the details of the acceleration mechanism. Particles might be advected fairly quickly into the jet lobe by hydrodynamic backflow, but this backflow slows and dissipates its energy through shocks or is broken up by vorticity and shear; as such, the flow gradually becomes slower and subsonic or transonic (e.g.

Falle 1991; Reynolds, Heinz & Begelman 2002; Matthews et al. 2019b). The lobe is therefore broadly characterized by transonic turbulence with bulk flows of  $u \sim c_s$ , where  $c_s$  is the sound speed. Flows can reach a significant fraction of  $c$  (Reynolds et al. 2002; Matthews et al. 2019b), implying a minimum advective time-scale  $\tau_{\text{adv}} \sim 100 \text{ kpc}/c_s \sim 1 \text{ Myr}$ . However, in practice, bulk flows are slower, and less uniform, at larger distances from the jet head, and even if the CRs are advected deep into the lobe it is not clear that this facilitates quicker CR escape. This argument depends on the details of the CR escape and the exact magnetic field structure in the lobe, particularly the degree of connectivity between the lobe field and surroundings, motivating further study. Generally, we expect the UHECRs to diffuse out of the lobes more quickly than they are advected away, and even in the case of being advected long distances they must still escape the turbulent cluster magnetic field. For our purposes, we assume that the CRs escape diffusively from the lobe.

We make a rough estimate of the escape time by assuming Bohm diffusion and using the magnetic field estimate described above. If Bohm diffusion applies, the escape time for ultrarelativistic particles of energy  $E$  and charge  $Ze$  from a sphere of radius  $L_s$  is given by

$$\tau_{\text{esc}}^{\text{cr}} = \frac{L_s^2}{2D_B} = \frac{3L_s^2}{2R_g c} = \frac{3L_s^2 Ze B}{2Ec}, \quad (12)$$

where  $D_B = R_g c/3$  is the Bohm diffusion coefficient and  $R_g$  is the Larmor radius. Our lobes are not spherical, so to quickly estimate the characteristic escape distance we approximate them as ellipsoids. The centre of mass of the lobes is at the origin, since we are assuming symmetrical jet propagation. The average distance to the lobe edge, which we take as a characteristic distance of escape, can then be calculated as  $L_{\text{esc}} = 2LK(m)/\pi$ . Here,  $L$  is the lobe length and  $K$  is the complete elliptic integral of the second kind (which ranges from 1 to  $\pi/2$  in this case).  $m = 1 - W^2/L^2$  is the square of the eccentricity and  $W$  is the lobe width, defined at the widest point, which is generally close to  $z = 0$ . Our final UHECR escape time estimate is

$$\tau_{\text{esc}}^{\text{cr}} = 9.05 \text{ Myr} \left( \frac{L_{\text{esc}}}{100 \text{ kpc}} \right)^2 \left( \frac{D_B}{D} \right) \left( \frac{E/Ze}{10 \text{ EV}} \right)^{-1} \left( \frac{B}{10 \mu\text{G}} \right). \quad (13)$$

We do not account for the magnetic field of the ambient medium or time delays introduced by diffusive propagation to Earth, but we discuss this and other limitations of our approach in Section 4.2.

## 2.6 UHECR and radiated luminosities

One of our aims is to examine the effect of jet variability on the particle populations in the lobe, as well any observational consequences for radio galaxies and UHECR origins. It is therefore useful to consider a few different (multimessenger) luminosities that are relevant for observers. We record the escaping UHECR luminosity and the radio luminosity due to synchrotron-emitting electrons, but also calculate the full broad-band SED at some time-steps. The UHECR luminosity at a given time can be calculated by integrating over the particle distribution for each species,

$$L_u(> E_u) = \sum_i \int_{E_u}^{\infty} \frac{En_i(E)}{\tau_{\text{esc}}^{\text{cr}}(E/Z_i)} dE, \quad (14)$$

or equivalently, by counting the number of CRs with  $E > E_u$  that leave the system in the solution of equation (9). We record the CR luminosity above 8 EeV, in order to compare to various studies of CR anisotropies, spectrum, and composition by the Pierre Auger

Collaboration (2017). We also record the full CR spectrum over time.

We calculate the synchrotron power per unit solid angle,  $P_v(\gamma_e)$ , where  $\gamma_e$  is the electron Lorentz factor, by assuming an isotropic pitch angle distribution (e.g. Crusius & Schlickeiser 1986; Ghisellini, Guilbert & Svensson 1988) and a single magnetic field strength throughout the lobe volume at a given time. The total synchrotron luminosity is then calculated by integrating over the electron population to find the synchrotron emissivity per unit solid angle,  $j_v$ , and multiplying by the volume of the lobe times  $4\pi$ , such that the specific luminosity is given by

$$L_v = 4\pi j_v V(t) = V(t) \int_{\gamma_0}^{\gamma_{\text{max}}} n_e(\gamma) P_v(\gamma_e) d\gamma_e, \quad (15)$$

where  $\gamma_0$  and  $\gamma_{\text{max}}$  are the minimum and maximum electron Lorentz factors. We record  $L_v$  at 144 MHz and 1.4 GHz for comparison with typical observation frequencies. We also present full broad-band SEDs in Section 3.4, calculated using GAMERA (Hahn 2015). We tested our synchrotron calculation against GAMERA and the SYNCH code from Hardcastle et al. (1998), finding excellent agreement.

Protons can produce gamma-rays via  $pp$  and  $p\gamma$  collisions. As above, we assume that the CMB and EBL radiation fields are dominant in our simulations. This assumption means that gamma-ray radiation from  $p\gamma$  interactions is negligible. The energy loss time-scale to  $pp$  collisions is  $\tau_{pp} \approx 600 (10^{-4} \text{ cm}^{-3}/n_p) \text{ Gyr}$  (Sikora et al. 1987), where  $n_p$  is the target proton density. The typical densities in our modelling are  $n_p \lesssim 10^{-5} \text{ cm}^{-3}$ , so we expect hadronic gamma-rays to be negligible and do not consider their contribution. We also checked, using GAMERA, that the luminosity from  $pp$  collisions was much lower than the IC contribution. However, we note that hadronic gamma-rays may be important either near the base of the jet or when the lobe densities and/or lobe energy contents are higher. In addition, it may be that densities are higher outside the lobe, or inside the lobe where there is significant mixing with the external medium due to, e.g. instabilities at the contact discontinuity. Hadronic gamma-rays could therefore feasibly be detectable from CRs in these regions.

## 3 RESULTS FROM A SINGLE, ILLUSTRATIVE JET MODEL

We produce results from a single jet history. We choose to model a light ( $\eta = 10^{-4}$ ) jet with a median (two-sided) jet power of  $Q_0 = 10^{45} \text{ erg s}^{-1}$  and a variability parameter of  $\sigma = 1.5$ . This median jet power is fairly typical of estimates for FR II radio galaxies, if slightly towards the lower end (Godfrey & Shabala 2013; Ineson et al. 2017). We chose these values of  $Q_0$  and  $\sigma$  to give reasonable overall energetics and dynamics for our source, but we also discuss the sensitivity to these parameters (as well as the PSD slope,  $\alpha_p$ ) in Section 4.5. The full set of parameters for this simulation, which we refer to as our *reference model*, is given in Table 1. We generate the synthetic jet power time series according to the procedure in Section 2.1 and evolve the jet until it is 300 kpc long. As the jet and lobe evolve, we record the various luminosities, lobe dimensions, lobe physical quantities, and time-scales as described in the previous section. The jet power time series is shown in Fig. 3, with an inset showing the resulting histogram of jet powers.

### 3.1 Time evolution of the system

In Fig. 4, we show the evolution of the important time-scales, dimensions, and physical quantities ( $B, n, P, \beta_j \Gamma_j$ ) from our reference simulated radio source. The UHECR escape time and adiabatic



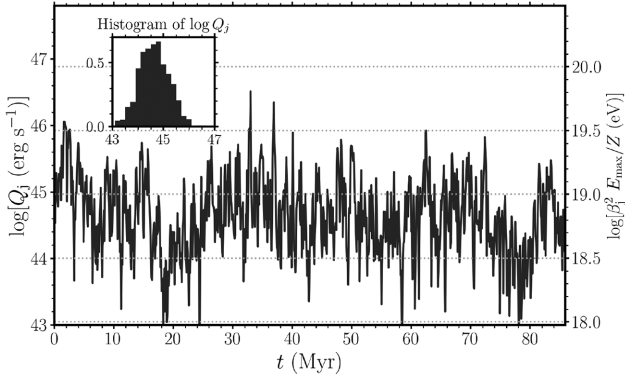


**Figure 3.** Jet power time series used for the reference model, with  $Q_0 = 10^{45} \text{ erg s}^{-1}$  and  $\sigma = 1.5$ . The jet power,  $Q_j$ , is shown on a log scale. For comparison,  $Q_j$  is also shown on a linear scale in the bottom panel of Fig. 4. The insets show the PSD used to generate the jet power time series and the resulting histogram of jet powers (with logarithmically spaced bins). On the right-hand y-axis, the corresponding value of  $\beta_1^2 E_{\text{max}}/Z$  is shown, for  $\epsilon_b = 0.1$  and  $\eta_H = 0.3$  (the parameters used in the simulation), with dotted horizontal lines marking 0.5 dex intervals. The right-hand axis is shown to give the reader a feel of the range of maximum energies protons can attain from a jet with these parameters, in the rough range from  $10^{18}$  to  $3 \times 10^{19} \text{ eV}$ .

cooling time are defined in the previous section, the synchrotron cooling time is denoted  $\tau_{\text{sync}}^e$ , and  $t$  is the age. We calculate  $\tau_{\text{sync}}^e$  for 1 GeV electrons and for electrons emitting with a characteristic frequency of 5 GHz, and give the CR escape time for 10 EeV protons. We also define the sound crossing time,  $\tau_{\text{cs}} = L/c_s$  where  $L$  is the lobe length and  $c_s \approx 700 \text{ km s}^{-1}$  is the sound speed in the (isothermal) ambient medium. Our reference model has a supersonic jet and its advance is also supersonic, so the longest time-scale in the system is generally  $\tau_{\text{cs}}$ . We do not show the IC cooling time, which, for 1 GeV electrons, is approximately 1.2 Gyr. This time-scale exceeds the longest synchrotron cooling time, as expected since  $U_B > U_{\text{CMB}}$  is always satisfied in this case. The particle acceleration time  $\tau_{\text{acc}}$  is not shown since this is always less than a few hundred years.

At early times ( $t \lesssim 5 \text{ Myr}$ ), the magnetic field is high ( $\sim 100 \mu\text{G}$ ) before gradually dropping to around  $10 \mu\text{G}$  at later times ( $t \gtrsim 60 \text{ Myr}$ ). The strength of the magnetic field is important because it sets the hierarchy of the UHECR escape time,  $\tau_{\text{esc}}^{\text{cr}}$ , and electron synchrotron cooling time,  $\tau_{\text{sync}}^e$ . Stronger (weaker) magnetic fields are better (worse) at confining UHECRs and cause quicker (slower) synchrotron cooling (see the next subsection). The UHECR escape time also depends on the size of the radio lobe. The strength of the magnetic field is proportional to the square root of the internal energy of the lobe; thus it is determined by a competition between the rate of change of volume and rate of change of energy. The former depends on the dynamics of the lobe, in particular the momentum flux, and the latter is equal to the jet power. Early on in the lobe's evolution, the environment is denser, so the relative change of volume for a given jet power is smaller. As a result, the magnetic field tends to decrease over time, because the lobe inflated by the jet finds it easier to expand. This behaviour is broadly consistent with the results of Croston, Ineson & Hardcastle (2018), who find higher mid-lobe pressures (for which we expect correspondingly higher B fields) in shorter lobes. We find that the length of the lobe increases faster than the width, meaning that the lobe aspect ratio – or axial ratio, both defined as length divided by width – increases over time, consistent with Blundell et al. (1999).

The jet lobe responds in a number of ways to the variability of the jet. Each time the jet power increases, the advance speed also increases, energy is injected more quickly into the lobe, and the particle populations are re-energized. The exact impact on a given quantity is complicated, because it depends on the relative importance of a given period of high activity compared to the overall history of the jet up to that point. Generally, each spike in jet activity causes a corresponding increase in synchrotron and UHECR luminosity, which then decays away with a characteristic response time set by the synchrotron cooling and UHECR escape time, respectively. This can be seen in Fig. 5. The effect of the cooling and escape times on the light curve is therefore to act as a ‘low-pass filter’; high-frequency variability is smoothed out and the power spectrum steepens above a temporal frequency  $f = 2\pi/\tau$ , where  $\tau$  is the relevant time-scale. This phenomenon has been discussed in the context of blazars by, e.g. Finke & Becker (2014) and Chen et al. (2016).

### 3.2 CR spectra and composition

Fig. 6 shows a number of different representations of CR spectra, in units of  $E^2 n(E)$  normalized to the maximum within the energy range  $10^{16} - 10^{21} \text{ eV}$ . The CRs that have not yet escaped from the lobe follow the  $n(E) \propto E^{-2}$  injection spectrum up to a characteristic break energy at which the escape time equals an effective source age. In contrast, the escaping CRs follow  $n(E) \propto E^{-1}$ , which peaks around the same characteristic break energy. The low-energy slope for the escaping CRs, which is dominated by the protons, is a result of the assumed rigidity-dependence of the diffusion coefficient, which we have set to the Bohm diffusion coefficient such that  $D_{\text{esc}} \propto E/Z$ . Both the internal and escaping spectra have a cutoff at higher energies. The rightmost panel of the Fig. 6 shows CR spectra from 30 random times throughout the simulation. There is significant diversity in the CR shape, particularly at high energies where the CRs can escape easily and are particularly sensitive to the recent activity of the jet. Below the spectral break, both the escaping and internal spectra behave in the same way as the time-averaged spectrum.

The CRs are split into different species, and a clear trend of heavier composition with increasing energy can be seen in both the internal and escaping CR spectrum. To illustrate this further, we show the value of  $\langle \ln A \rangle$ , the mean of the natural logarithm of the atomic mass number contributing to a given energy bin, in Fig. 7. Both CR acceleration and CR escape are rigidity-dependent rather than energy-dependent; as a result the value of  $\langle \ln A \rangle$  naturally increases with energy. In the case of the CRs internal to the lobe, higher energies will exceed the CR energy at which light species have already escaped the lobe. In the case of the escaping CR, higher energies will exceed the maximum CR energy for light species. There is therefore a subtle difference between the increasing value of  $\langle \ln A \rangle$  for the escaping and internal CRs. The fact that the escaping CRs have a lighter composition can be understood in two ways. First, that at a given  $E$ , CRs with lower  $Z$  have a higher rigidity and so find it easier to escape. Alternatively, one can think of the energy difference between the curves in Fig. 7 as encoding the difference between the characteristic maximum energy and the characteristic energy of escaping CRs. The difference between these is maximized when  $E_{\text{max}}/Z \rightarrow \infty$  and minimized when the source lifetime is comparable to the escape time for CRs of rigidity  $E_{\text{max}}/Z$ .

The abundances of species outside the source environment itself is dictated by the transport properties in this external region. In the case where energy dependent transport dominates (as may be expected if particles propagate diffusively), the resulting composition will change. Specifically, there will be an enhancement of

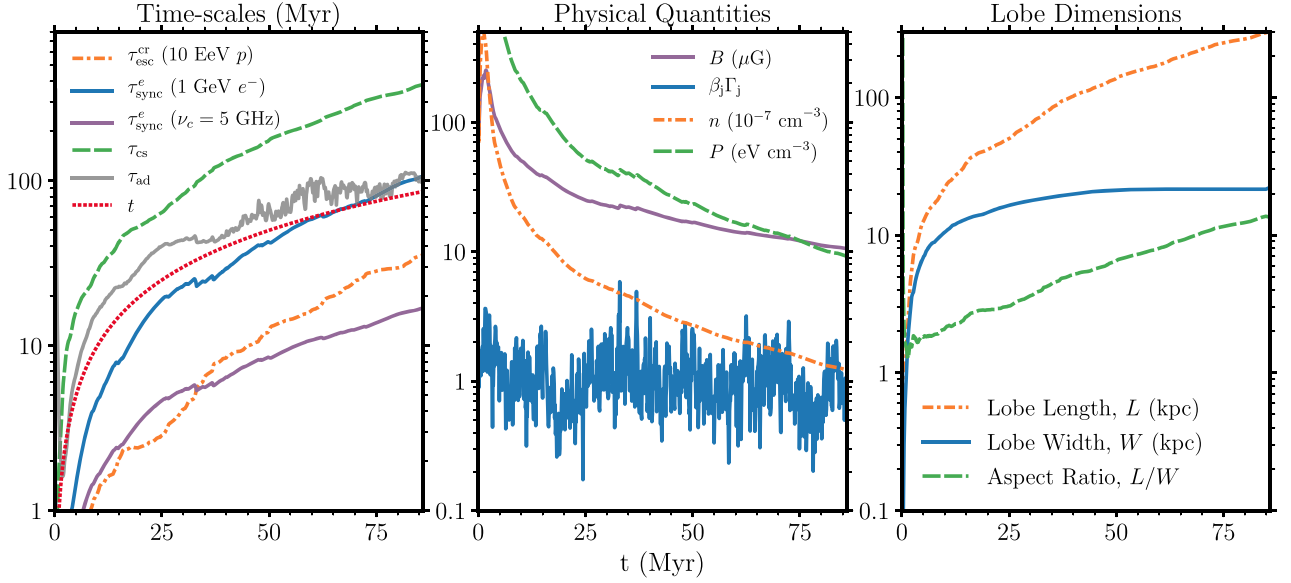


**Figure 4.** The time evolution of the time-scales, physical quantities, and dimensions of the lobe in the reference simulation. Each plot is shown on a logarithmic y-axis with the same scale on the x-axis. *Left:* The sound-crossing time, source age, UHECR escape time, adiabatic cooling time, and synchrotron cooling time as a function of time. We give the synchrotron cooling time for 1 GeV electrons and for electrons emitting with a characteristic frequency of 5 GHz. *Centre:* The lobe magnetic field strength,  $B$ , lobe density,  $n$ , lobe pressure,  $P$ , and jet Lorentz factor (multiplied by  $\beta$ ) as a function of time. *Right:* The length, width, and aspect ratio of the radio source over time. The aspect ratio is defined as the length divided by the width.

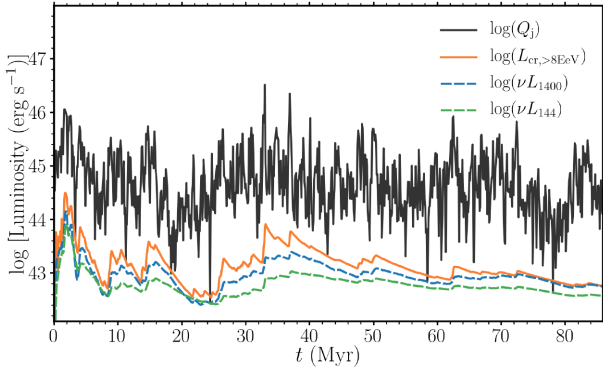


**Figure 5.** The evolution of the various luminosities over time in the reference simulation. The jet power is shown in black, matching Fig. 3. The UHECR luminosity is calculated above 8 EeV for comparison with studies from the Pierre Auger Observatory, and the radio luminosity is given in  $\nu L_\nu$  units for observation frequencies of 144 and 1400 MHz.

heavy species outside the source; this effect is discussed further in Section 4.2.

### 3.3 The CR cutoff

In our modelling, we apply an exponential cutoff with a maximum energy that is proportional to  $\sqrt{Q_j/\beta_j}$  (equation 11), as derived from the Hillas condition. As the jet power varies, so does this maximum energy (see Fig. 3); in more powerful episodes, both the maximum energy and normalization associated with the source term increases, as can be seen in the range of cut-off energies in the spectra at random times shown in Fig. 6. To gain more insight into the problem, we consider the total integrated spectrum (both internal and escaped CRs) and neglect the  $n_i/\tau_{\text{loss}}$  term. In this limit, the total spectrum

is the integral of the source term, i.e.  $n_i(E) = \int_0^{\Delta t} S_i(E/Z_i, f_i, t) dt$ , where  $\Delta t$  is the outburst time. In the limit of large  $\Delta t$ , and setting  $\beta_j = 1$  for simplicity, it can be shown that (see Appendix B)

$$n_i(E) \propto \int_0^\infty p(Q_j) Q_j \exp\left(-\frac{E}{k_E \sqrt{Q_j}}\right) dQ_j, \quad (16)$$

where  $k_E = \eta_H Z_i \sqrt{\epsilon_b}$  is the constant of proportionality in the maximum energy equation. We have written this using a general PDF  $p(Q_j)$  so that it can be applied to other situations where the PDF of input powers takes a different form. The specific form of equation (16) for our adopted lognormal  $p(Q_j)$  is

$$n_i(E) \propto \int_0^\infty \frac{1}{\sigma \sqrt{2\pi}} \exp\left[-\frac{E}{k_E \sqrt{Q_j}} - \frac{(\ln(Q_j/Q_0))^2}{2\sigma^2}\right] dQ_j. \quad (17)$$

This integral is not analytically straightforward, but a very good approximation can be obtained by considering only the peak of the integrand (see Appendix B). The general behaviour can already be appreciated from equation (16): a spread in jet powers acts to stretch out the exponential cutoff in the spectrum, such that the cut-off function is the convolution of the jet power PDF and the source term cutoff. The effect is similar in nature to the convolution of a CR source term with a luminosity function, and a comparable discussion in the context of supernova remnants (SNRs) is given by Shibata et al. (2010). The fact that the source term normalization is proportional to  $Q_j$  biases the spectrum towards higher energies, even for a symmetric PDF. This effect is even more pronounced if  $p(Q_j)$  is positively skewed as is the case for a lognormal distribution. The result is that the most important episode of activity for determining the CR maximum energy cutoff is likely to be the most energetic episode that has occurred within a UHECR loss time.



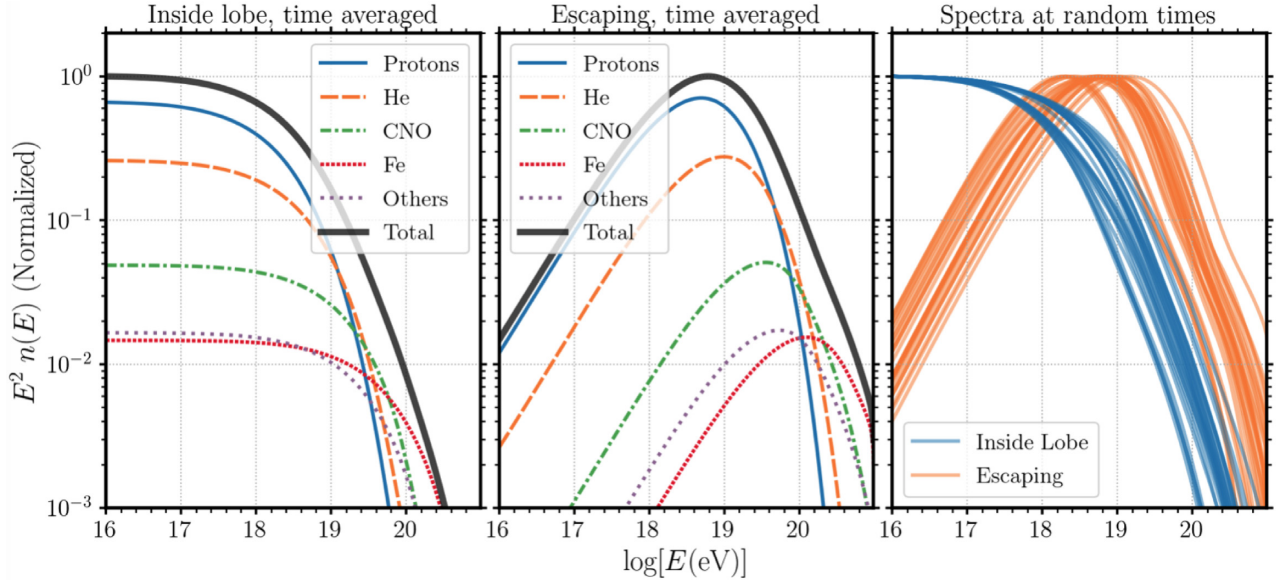


**Figure 6.** CR spectra from the reference simulation, in  $E^2 n(E)$  units where  $n(E) = dN/dE$  is the differential spectrum; an  $E^{-2}$  CR spectrum appears as a horizontal line. *Left:* The CR spectra inside the lobe averaged over the jet history. The thick black line shows the total CR spectrum, and the coloured lines show the contributions of individual species. The spectral shape matches the injected spectrum up to a characteristic break energy, beyond which the spectrum steepens due to the escape of high-energy CRs. *Centre:* As in the left-hand panel, but for the CRs escaping the lobe. The CR spectra behaves in an opposing manner to the left-hand panel, with an inverted spectrum below a characteristic energy, and a flat  $\sim E^{-2}$  spectrum above this energy. The spectrum steepens above a break energy determined by the range of maximum energies during the simulation due to the variable jet power; the shape of this cutoff is discussed further, for an idealized case, in Section 3.3. *Right:* CR spectra from 50 random times during the simulation. Broadly speaking, the spectra are similar to the averaged spectrum, except that jet variability causes the location of the maximum energy cutoff for the escaping CRs to jump around over time. In addition, the value of  $\tau_{\text{esc}}^{\text{cr}}$  increases over time as the lobe becomes larger, which changes the break energy for the CRs inside the lobe and the peak in the escaping spectrum.

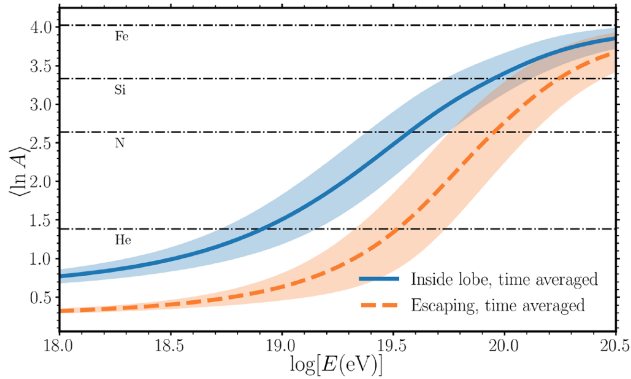


**Figure 7.** The value of  $\langle \ln A \rangle$  as a function of energy in the simulation. Solid and dashed lines show the mean value across the jet history, and the shaded region shows the standard deviation at each value of  $E$ . The CR escape time is a rigidity ( $E/Z$ ) dependent quantity, so at a given energy lighter species find it easier to escape due to their lower  $Z$ . This means that the escaping CRs (orange) have a lighter composition than the CRs remaining inside the lobes (blue).

### 3.4 Spectral energy distribution

In Fig. 8, we show broad-band SEDs at 10 Myr intervals throughout the jet history. The SEDs are calculated using GAMERA as described in Section 2.6. Each curve is colour coded according to the elapsed time, and the inset axis shows the corresponding electron spectra. The top panel shows the jet power over time, as in Fig. 3, but with the time intervals marked with vertical dashed lines to aid interpretation of the plot. We also show characteristic observing frequencies for radio and

X-ray, as well as for the *Fermi Large Area Telescope (Fermi-LAT)* with coloured horizontal bands.

The SED is characterized by a classic double-humped shape, with the low-energy bump caused by synchrotron emission and the high-energy bump caused by IC scattering off the CMB. We also computed the spectrum from  $pp$  collisions but found it was insignificant due to the low density of target protons in the lobes. Although a double-humped SED shape is often associated with blazars (e.g. Fossati et al. 1998; Ghisellini et al. 1998), it is a generic feature of a population of electrons interacting with magnetic fields and radiation fields when the energy densities of the two fields are comparable. For IC scattering in the Thomson regime, the relative contribution of the synchrotron and IC processes is given by the ratio of the relevant energy densities ( $U_B$  and  $U_{\text{CMB}}$  in this case). In the reference model,  $U_B > U_{\text{CMB}}$  at all times, and the decrease of  $B$  over time causes the synchrotron bump to be more dominant at early times compared to late times.

There are clear kinks and inflection points in both the SED and electron spectrum (inset). A correspondence can be seen between features in the synchrotron hump and both the IC hump and the electron spectrum, as expected, although some of the smaller features in the electron spectrum are smoothed out in the SED since each electron energy range produces radiation over a broader range of frequencies. The kink and inflection features are caused by the variability of the jet; effectively, the result is a ‘many-populations’ model where the electron spectrum is a series of injected populations that have each been subjected to a different cooling history. The behaviour of the electron spectrum can be understood further as follows. If a given short period of high activity dominates over the integrated historical energy input of the jet, the system behaves like a system in ‘outburst’, and the spectrum resembles that of a single power-law

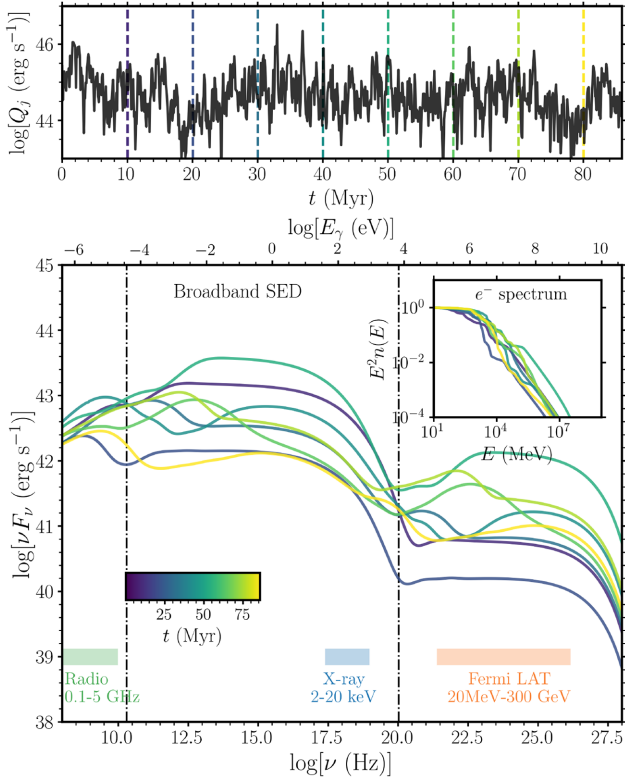


**Figure 8.** The effect of jet variability on the broadband SED. *Top:* Jet power time series, as in Fig. 3, with 10 Myr intervals marked by dotted lines with colours corresponding to the colours used in the bottom panel. *Bottom:* Broad-band SED at the same 10 Myr intervals throughout the jet history, shown in  $\nu F_\nu$  units and with photon frequency and energy marked on separate axes. The colour coding denotes the time in Myr at which the spectrum is calculated. Typical observational frequency ranges for radio (0.1–5 GHz), X-ray (2–20 keV), and *Fermi* LAT (20 MeV–300 GeV) are marked with coloured bands. The dot-dashed vertical lines mark the frequencies at which the ‘proxy electrons’ (electrons cooling at the same rate UHECRs are escaping) emit their synchrotron and IC radiation (see Section 4.1). *Inset:* The corresponding electron spectrum in the same colours and in units of  $E^2 n(E)$ . The dot-dashed vertical lines mark the energy of the proxy electrons discussed in Section 4.1.

spectrum with a cooling break. However, in some circumstances, the period of high activity can only really be seen at high frequencies or particle energies; this is because the low-energy particles have not had time to cool and so still reflect the integrated activity, whereas the high-energy particles (above the cooling break) from previous activity have all cooled, and the new powerful episode injects fresh particles in this regime that can radiate. As a result, a characteristic spectral shape is seen, with inflection points and a secondary peak and break associated with the recent ‘outburst’, leading to a spectral hardening in the spectrum. A similar result is found by Turner (2018), who refers to the spectral hardening as a ‘steep-shallow’ spectrum produced by a source with short distinct outbursts. This spectral hardening effect could be an important signature of variability, so we discuss the observational perspective in Section 4.3.

## 4 DISCUSSION

### 4.1 Which photon frequencies track the UHECR escape time?

From Fig. 5, we can see that the radio and UHECR luminosities respond to impulses from the jet with a decay time set by the synchrotron cooling and CR escape times, respectively. We can

therefore calculate at which electron energy the electrons are cooling at the same rate that the UHECRs are escaping; we refer to the electrons at this energy as ‘proxy electrons’ for the UHECRs. These proxy electrons emit their synchrotron and IC radiation at characteristic frequencies in radio and higher energy bands. These radiation frequencies can be determined by comparing the UHECR escape time to the relevant cooling times. The characteristic frequency of synchrotron emission from an electron with Lorentz factor  $\gamma_e$  can be conveniently written in terms of the Schwinger field such that

$$\nu_c = \gamma_e^2 \left( \frac{B}{B_{\text{crit}}} \right) \frac{m_e c^2}{h}. \quad (18)$$

Similarly, we can write the synchrotron cooling time as

$$\tau_{\text{sync}}^e = \frac{9}{4\alpha} \left( \frac{B_{\text{crit}}}{B} \right)^2 \frac{\hbar}{\gamma_e m_e c^2}. \quad (19)$$

We can combine these two expressions and eliminate the  $\gamma_e$  dependence so that

$$\tau_{\text{sync}}^e \approx 41 \text{ Myr} \left( \frac{B}{10 \mu\text{G}} \right)^{-3/2} \left( \frac{\nu_c}{\text{GHz}} \right)^{-1/2}. \quad (20)$$

Finally, equating this with equation (13) and rearranging for frequency gives

$$\nu_{\text{proxy}} \approx 20 \text{ GHz} \left( \frac{E/Z e}{10 \text{ EV}} \right)^2 \left( \frac{L_{\text{esc}}}{100 \text{ kpc}} \right)^{-4} \left( \frac{D_{\text{esc}}}{D_B} \right)^2 \left( \frac{B}{10 \mu\text{G}} \right)^{-5}. \quad (21)$$

This is the characteristic frequency of synchrotron radiation emitted by the proxy electrons, which cool at the same rate that UHECRs of rigidity  $E/Z e$  escape from the lobe. Unfortunately, this equation is extremely sensitive to many of the parameters, particularly the magnetic field. Decreasing the magnetic field by a factor of 10 changes  $\nu_{\text{proxy}}$  by a factor of  $10^5$ , which shifts the observing window from the radio to the far-infrared ( $\sim 15 \mu\text{m}$ ). The corresponding IC emission from such ‘proxy electrons’ is

$$E_\gamma^{\text{IC}} = \left[ \frac{E_\gamma^{\text{CMB}}}{(B/B_{\text{crit}}) m_e c^2} \right] h \nu_{\text{proxy}} \quad (22)$$

$$\approx 0.44 \left( \frac{E_\gamma^{\text{CMB}}}{6 \times 10^{-4} \text{ eV}} \right) \left( \frac{10 \mu\text{G}}{B} \right) \left( \frac{\nu_{\text{proxy}}}{20 \text{ GHz}} \right) \text{ MeV}. \quad (23)$$

We have marked both  $\nu_{\text{proxy}}$  and  $E_\gamma^{\text{IC}}/h$  with vertical dot-dashed lines in Fig. 8. For these specific parameters, the IC emission from the proxy electrons falls in the  $\sim \text{MeV}$  range, at lower energies than probed by current gamma-ray telescopes such as *Fermi* LAT. The similarity of the features in the SED at  $\nu_{\text{proxy}}$  and  $E_\gamma^{\text{IC}}/h$  is apparent – whenever a kink or feature occurs in the synchrotron curve at  $\nu_{\text{proxy}}$  a matching one is seen in the IC bump, confirming that the two frequencies correspond to electrons of the same energy.

The results of this section are summarized in Fig. 9, where we show a comparison of synchrotron cooling times and UHECR escape times as a function of  $B$  for some appropriate parameter values. To give a feel for typical magnetic fields in radio galaxy lobes, we also show the interquartile range (IQR) of observational estimates of  $B$  from table 9 of Croston et al. (2005). Our reference model has higher magnetic fields than these observational estimates at early times but at late times the  $B \sim 10 \mu\text{G}$  fields fall within this range. Fig. 9 can be thought of as a graphical representation of the simple derivation above; longer CR escape times (from larger lobes, higher  $B$ , or slower transport) are tracked by proxy electrons with longer synchrotron cooling times, so the value of  $\nu_{\text{proxy}}$  decreases as  $\tau_{\text{esc}}^{\text{CR}}$  increases.

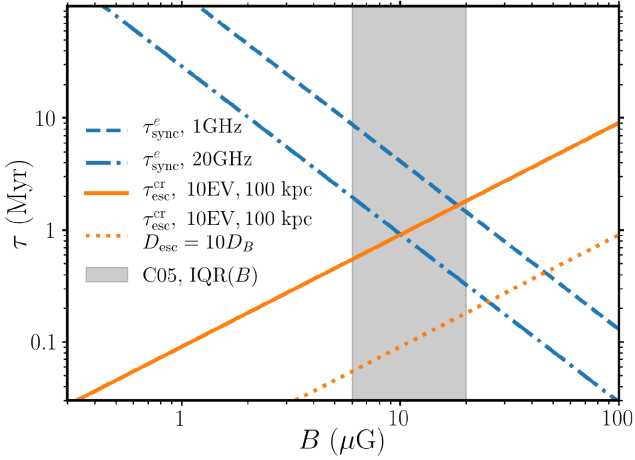


**Figure 9.** A comparison of the synchrotron cooling time,  $\tau_{\text{sync}}^e$ , and CR escape time,  $\tau_{\text{esc}}^{\text{cr}}$ , as a function of  $B$ . We show  $\tau_{\text{sync}}^e$  at two different frequencies, compared to estimates of  $\tau_{\text{esc}}^{\text{cr}}$  for two different escaping diffusion coefficients.  $\tau_{\text{esc}}^{\text{cr}}$  is calculated for  $L_{\text{esc}} = 100$  kpc and  $E/Ze = 10$  EV. The Bohm diffusion estimate intersects with the 20 GHz synchrotron curve at  $B \approx 10$   $\mu\text{G}$ . We also show, in a grey band, the IQR of observational estimates of  $B$  from Croston et al. (2005, C05, their table 9).

The above derivation is carried out for a given CR energy, but an alternative approach is to assume that the UHECRs have reached the Hillas energy,  $E_H = \beta BLZe$ . However, it is important to draw a distinction here between the conditions in the accelerator and the conditions when the CRs are escaping. We might expect the acceleration site to be close to the hotspot, for example in secondary shocks near the jet head (e.g. Matthews et al. 2019b), where the characteristic velocities and magnetic field strengths are higher than the average values in the lobe. Bell, Matthews & Blundell (2019) showed that acceleration by multiple shocks in radio galaxy backflows provides a mechanism to reach close to the Hillas energy ( $E_{\text{max}} \approx 0.6E_H$ ). One advantage of these backflows is that they are not highly relativistic, thus the difficulties associated with UHECR acceleration at relativistic shocks (Lemoine & Pelletier 2010; Reville & Bell 2014; Bell et al. 2018) can be avoided. Let us denote the magnetic field strength, velocity, and size scale of the acceleration site as  $B_{\text{acc}}$ ,  $\beta_{\text{acc}}$ , and  $L_{\text{acc}}$ , respectively. We can then use the Hillas energy to write the escape time in terms of the ratios of these quantities to the lobe values, that is

$$\tau_{\text{esc,H}}^{\text{cr}} \approx 24.5 \text{ Myr} \left( \frac{L_{\text{esc}}/L_{\text{acc}}}{50} \right) \left( \frac{B/B_{\text{acc}}}{0.1} \right) \left( \frac{L_{\text{esc}}}{100 \text{ kpc}} \right) \times \left( \frac{\beta_{\text{acc}}}{0.1} \right)^{-1} \eta_H^{-1}, \quad (24)$$

where we have used some characteristic values assuming the UHECRs are accelerated in non-relativistic ( $\beta_{\text{acc}} \sim 0.1$ ) backflow shocks that are smaller than  $L_{\text{esc}}$  by a factor of 50 but also have stronger magnetic fields than in the lobes by a factor of 10, based on results from Matthews et al. (2019b).

#### 4.2 Extragalactic CR transport

We have studied how CR diffusion out of the lobes affects the escaping composition, spectrum, and luminosity over time, but we have not accounted for the propagation time of the CRs through extragalactic and Galactic magnetic fields, or the resulting effect on CR composition. Deflection in the extragalactic magnetic field

(EGMF) introduces a time delay relative to rectilinear propagation or light travel. This delay is in addition to the escape time from the source, such that the total delay relative to the radiative signatures is  $\tau_{\text{tot}} = \tau_{\text{esc}}^{\text{cr}} + \tau_{\text{prop}} - (R/c)$  for a source at distance  $R$ , where  $\tau_{\text{prop}}$  is the propagation time (outside the lobe) and we assume  $R \gg L_{\text{esc}}$ . The propagation time depends on the diffusion coefficient as  $\tau_{\text{prop}} \sim R^2/D$ . For the rest of this discussion, we assume that the scattering length is small compared to the source distance,  $R > D/c$ . The rigidity dependence of the diffusion coefficient depends on the ratio of the Larmor radius to the coherence length of the magnetic field,  $\lambda_c$  (see Guedes Lang et al. 2020, their equation 1). For low rigidity particles,  $R_g < \lambda_c$ , the propagation is diffusive with  $D \propto R_g^{1/3} \lambda_c^{2/3}$ , resulting in the expression

$$\tau_{\text{prop}} \sim 0.7 \text{ Gyr} \left( \frac{E/Ze}{0.1 \text{ EV}} \right)^{-\frac{1}{3}} \left( \frac{B}{1 \text{ nG}} \right)^{\frac{1}{3}} \left( \frac{\lambda_c}{1 \text{ Mpc}} \right)^{-\frac{2}{3}} \times \left( \frac{R}{10 \text{ Mpc}} \right)^2, \quad (25)$$

where we have chosen values such that the  $R_g < \lambda_c$  regime applies. This propagation time here can be extremely long, but since in an nG-strength EGMF the Larmor radius of a 1 EV rigidity CR is 1.08 Mpc, the above regime is only realized for very large coherence lengths or particle rigidities below 1 EV. For rigidities above 1 EV, we generally expect  $R_g > \lambda_c$  in the EGMF, and we instead obtain

$$\tau_{\text{prop}} \sim 0.28 \text{ Gyr} \left( \frac{\lambda_c}{1 \text{ Mpc}} \right) \left( \frac{E/Ze}{10 \text{ EV}} \right)^{-2} \left( \frac{R}{100 \text{ Mpc}} \right)^2 \left( \frac{B}{1 \text{ nG}} \right)^2, \quad (26)$$

where the field is assumed to be random and turbulent. For smaller  $R$ , such that  $R < D/c$ , an expression of similar form to equation (26) can be obtained in the small-angle scattering limit. The above estimates vary depending on the exact numerical prefactors adopted.

Time delay effects have been discussed in the context of variable UHECR sources with reference to transient sources such as GRBs; Miralda-Escude & Waxman (1996) show that the observed UHECR spectrum of a transient or ‘bursting’ source tends to peak at the UHECR energy where  $\tau_{\text{prop}}$  is equal to the time since photon arrival. The basic principle is similar to the idea of ‘proxy electrons’ we introduced in Section 4.1, except that in the case of a flickering source the particles are accelerated over many episodes rather than in a transient burst or impulse. A further time delay can be introduced by the escape from the environment surrounding the source – for example, the CRs might have to escape from a cluster. CR escape from cool-core clusters has been studied by Kotera et al. (2009), with typical magnetic field strengths of 10  $\mu\text{G}$  in the cluster leading to escape times comparable to those considered here. The estimates here are uncertain, but they show that the propagation times are of larger or comparable magnitude to the escape time from the lobes for CRs with  $> \text{EV}$  rigidities, propagating in  $\sim 1$  nG fields for sources within  $\sim \text{tens}$  of Mpc. The propagation time is significantly shorter if the source distance becomes comparable to the scattering length. Any additional delay modifies the equations in Section 4.1 and implies that lower energy proxy electrons may be more appropriate as tracers of the propagating UHECRs. At lower CR rigidities and for larger source distances, the propagation times quickly become restrictive with respect to typical source lifetimes.

Diffusive propagation in the extragalactic region between the source and the Milky Way will lead to the CR density to accumulate due to the increased CR residence time in this region. Assuming the propagation is purely diffusive, once the steady-state level is reached, the CR density from a single source of distance  $R$  will sit at a factor of



( $Rc/D$ ) larger than the CR flux level from the source. Assuming that the rigidity dependence of the diffusion takes the form  $D \propto (E/Z)^\delta$ , with  $\delta > 0$ , rigidity dependent build up will occur. Subsequently, the steady-state density for CRs of the same energy will have heavier species abundance enhanced relative to light species, when compared to the escaping species abundance ratio from the source.

### 4.3 Observational applications

Observations of radio galaxies commonly reveal complex radio morphologies and evidence for restarting or episodic activity. In addition to these morphological signatures, our work demonstrates the potential of spectral signatures as probes of variability. In particular, inflection points where the spectrum is a sum of two or more components with different cooling breaks can be a signature of variability and a recent ‘outburst’ (Section 3.4). Related behaviour is seen in Fornax A; Maccagni et al. (2020) find that the central unresolved component has a spectral break at a higher frequency than for the outer lobes, suggesting a recent injection of fresh non-thermal electrons consistent with a jet power varying on Myr time-scales. Spectral hardening in gamma-rays could also be a potential signature of variability, as has been observed at GeV photon energies in Centaurus A (Abdalla et al. 2020). Variability in radio galaxies could also be important when determining the ages of the sources. There is often a discrepancy between the measured spectral age of a source (as measured from the synchrotron break frequency) and the dynamical age, known as the ‘spectral age problem’ (Eilek 1996; Harwood et al. 2013; Harwood, Hardcastle & Croston 2015). This problem can be alleviated if the magnetic field is below equipartition (Mahatma et al. 2020). Jet power variability can also help solve the spectral age problem in a few different ways. First, a recent injection of fresh non-thermal electrons could lead to the spectral age being measured as much smaller than the true age of the source. Secondly, a series of powerful episodes can cause the source to grow faster (advance more quickly) than if the source had a steady jet with a power equal to the median or mode of the jet power history, resulting in a measured dynamical age much longer than both the true age and typical synchrotron age of the non-thermal electrons.

Based on our modelling, we can also identify a number of interesting areas of the synchrotron and IC spectra that may provide further clues about particle acceleration and jet variability. In the gamma-rays, we suggest that characterizing, in detail, the steepening of the spectrum associated with the cooling of electrons could be used to search for spectral hardening indicating recent jet activity. Observations close to the frequencies associated with proxy electrons could also be useful for predicting UHECR luminosities from individual objects although, as we have shown, the appropriate frequency for the proxy electrons is strongly dependent on the CR transport.

Additionally, we note that our work has some implications for AGN more generally, in the context of accretion modes and radio properties of quasars. Long-term accretion variability is likely to be important for explaining why quasars with nearly identical emission-line properties can have very different radio properties (Richards et al. 2011; Rankine et al., submitted). Such a characteristic can be partly explained by a disconnect between the properties of the quasar accretion disc and the non-thermal electrons, as expected if the synchrotron cooling time is longer than the time-scale over which the quasar changes its ultraviolet/optical properties. A similar principle might also be applied to the high-/low-excitation radio galaxy (HERG/LERG) dichotomy, which classifies radio galaxies based on the presence or otherwise of strong optical emission lines (Laing et al. 1994; Tadhunter et al. 1998; Best & Heckman 2012).

The HERG/LERG distinction is thought to be fundamentally driven by Eddington fraction and accretion mode (Best & Heckman 2012), but the two classes are found across a wide range of luminosities. The optical emission lines would be expected to respond on shorter time-scales than the radio, so it is plausible that some HERGs and LERGs are similar objects, but with the disc caught in different states; for example, HERGs could correspond to objects that have recently (within a synchrotron cooling time) transitioned into a radiatively efficient state. A refinement to our model would be needed to investigate this in more detail; we create a synthetic jet power time series, but one could determine the jet power from an underlying accretion model with different modes of fuelling. Future work in this area might focus on incorporating particle acceleration physics into numerical simulations that simultaneously model the fuelling of the AGN as well as the resulting jet (e.g. Yang & Reynolds 2016; Beckmann et al. 2019).

### 4.4 Parallels with Galactic accelerators

There are important parallels to draw between radio galaxy models for UHECRs and the phenomenology of Galactic CRs. Galactic CRs up to the knee are thought to be accelerated in the shocks of SNRs, although reaching to PeV energies is a challenge and requires (at least) significant CR-driven magnetic field amplification (Bell et al. 2013; Blasi 2013; Bell 2014). Jets in X-ray binaries might also contribute, particularly at the high-energy end (Heinz & Sunyaev 2002; Fender, Maccarone & van Kesteren 2005; Cooper et al. 2020), and the discovery of TeV gamma-rays from SS433 indeed suggests that X-ray binary jets might be good high-energy CR accelerators (Abeysekara et al. 2018). Within the SNR paradigm for Galactic CRs, the most energetic galactic CRs are thought to come from young SNRs with fast-moving shocks, with the bulk of the lower energy CRs originating from older, more numerous SNRs and forming a near isotropic ‘soup’. As a result, it is natural that stochasticity becomes important at CR energies close to the knee (e.g. Blasi & Amato 2012a,b), because the number of sources capable of reaching these energies is relatively small. Can similar behaviour be invoked at ultrahigh energy? Nearby radio galaxies are compelling sources for explaining the UHECR spectrum and anisotropies at extreme ( $\gtrsim 10$  EeV) energies (Eichmann et al. 2018; Matthews et al. 2018; Eichmann 2019b; Guedes Lang et al. 2020). At lower energies (0.1 to a few EeV) the energy loss length-scales from the GZK effect and photodisintegration are larger. Thus, the CRs in this energy range could instead come from an ensemble of background radio galaxies as discussed by Eichmann (2019a) and Matthews et al. (2019b), forming a roughly isotropic component with a spectrum largely determined by the integrated radio galaxy luminosity function. This isotropic component would still have to be produced in relatively local sources, since the propagation times impose a magnetic horizon at low rigidities, as can be seen from inspection of equation (25). The overall importance of stochasticity in determining the UHECR spectrum is emphasized by the fact that the very same nearby radio galaxies that are often invoked as UHECR sources also show evidence for variable jet powers, a complex merger history, and unusual radio lobe morphologies.

### 4.5 Model limitations, parameter sensitivity, and future work

Our modelling approach is relatively simple and heuristic, and there are a number of physical characteristics of lobes and jets that are not well modelled by our scheme. We have already discussed CR transport. Another limitation is the treatment of the lobe as a single, uniform bubble, when in reality there is a complex interplay between



the jet head, the jet itself, and the lobe (e.g. Falle 1991), and the hotspot is significantly higher pressure than the rest of the lobe. Our assumption affects the observed integrated spectrum, but also the cooling history of the electrons. A future model might include two or more ‘zones’, with particles gradually moved from the ‘hotspot’ population to the lobe at an appropriate advective rate. A technique like this has been applied in the RAiSE semi-analytical models (Turner et al. 2018). Alternatively, magnetohydrodynamic simulations using tracer particles to model ensembles of electron could be used to account for the mixing of populations and non-uniformity of the magnetic field; Vaidya et al. (2018) describe a recent implementation in the hydrodynamics code PLUTO (Mignone et al. 2007).

We have chosen to present results from one jet model, and the specific jet power time series chosen will clearly affect the results. Even the random number seed changes the exact jet power history, but it is more relevant to focus on the fundamental parameters of the time series: the variability parameter,  $\sigma$ , the PSD slope,  $\alpha_p$ , and the median jet power,  $Q_0$ . Increasing the median jet power increases the typical maximum CR energy attainable in the accelerator (from equation 11). As a result, the spectra shift to the right in Fig. 6. The effect on the magnetic field is more nuanced. The magnetic energy being injected into the lobes increases with  $Q_0$ , but the energy density of the lobes also depends on the rate of change of lobe volume, and is expected to increase as  $Q_0$  raised to an exponent  $< 1$ . We therefore expect the magnetic field to be stronger in the lobes of more powerful sources, leading to slower CR escape and faster synchrotron cooling. Adopting a higher  $\sigma$  makes the jet power PDF more skewed, such that the mean jet power is higher compared to  $Q_0$ . However, increasing  $\sigma$  also increases the amplitude of variability, which has the effect of exacerbating variability signatures in the time evolution (Figs 4 and 5) and broad-band SED (Fig. 8). Changing the shape of the PDF would also have a profound effect, with more symmetric distributions (e.g. a Gaussian) qualitatively mimicking the behaviour of a low  $\sigma$ , and more asymmetric or skewed distributions increasing the difference between the mean and median  $Q_j$ . Finally, we consider the PSD slope,  $\alpha_p$ . The pink/flicker noise PSD we used ( $\alpha_p = 1$ ) puts equal power in each logarithmic frequency range. A steeper PSD slope,  $\alpha_p > 1$ , leads to more power in low-frequency modes. For  $\alpha_p = 2$ , the time series behaves as red noise and follows a random walk. As a result, once the jet enters a high state, it tends to stay there for longer. This behaviour could in principle lead to more dramatic signatures in the UHECR luminosity or calculated spectra. The spectrum would be more sensitive to the exact location in the time series, with longer time-scale trends apparent in the luminosities and composition, and the opposite being true for a flatter PSD slope.

There are numerous other parameters that are important, such as the energy partitioning factors ( $\epsilon_b$ ,  $\epsilon_e$ ,  $\epsilon_c$ ) and the particle spectral index,  $p$ . The particle spectral index is particularly important for the UHECR luminosity. Our chosen value of  $p = 2$ , the canonical value for shock acceleration (Bell 1978), spreads out the total energy equally in each decade of energy, but there are many reasons to expect steepening of the CR spectrum (e.g. Bell et al. 2019). Even a mild steepening to  $p = 2.1$  causes (for a single specie) the fraction of total CR energy contained in UHECRs above 8 EeV to drop to  $\approx 2.5$  per cent (compared to  $\approx 10$  per cent for  $p = 2$ ). Finally, we note that our assumptions about the maximum particle energy could be relaxed in future work. In particular, we assumed a constant maximum electron energy,  $E_{\max,e}$ , but it would be interesting to investigate the impact of a power-dependent  $E_{\max,e}$ , obtained by balancing the electron acceleration time with the synchrotron time in the amplified magnetic field in the jet hotspot. The value of  $E_{\max,e}$

primarily affects the shape of the SED in Fig. 8. It may also be necessary to account for more detailed plasma physics for both electrons and CR ions, since, particularly in relativistic shocks, the growth rate of CR-driven turbulence at the shock can be severely limiting in terms of the maximum particle energy (e.g. Reville & Bell 2014; Araudo et al. 2016, 2018; Bell et al. 2018).

## 5 CONCLUSIONS

We have presented a study of particle acceleration in radio galaxies with jet powers that vary over time according to a flicker noise power spectrum, and examined the effect of this flickering on the UHECR and electron populations accelerated by the source. Our main conclusions are as follows:

(i) A lognormal distribution of jet powers results in a mean jet power that is significantly higher than the median, and especially, the mode (Fig. 1). If such a distribution is realized on long time-scales ( $\gtrsim \text{Myr}$ ) in nature, it provides a situation where UHECRs can be accelerated in the most powerful episodes, even when the most commonly observed jet power is significantly lower. This is true more generally for positively skewed PDFs for the jet power and could also apply to systems that undergo distinct outbursts.

(ii) We present a semi-analytical model for studying the evolution of radio jets and lobes and the particle populations they accelerate and contain (Section 2). Our model is influenced by other semi-analytical approaches (e.g. Hardcastle 2018; Turner et al. 2018), but explicitly accounts for a variable power, transrelativistic jet, and also models the non-radiating CR ion populations and their diffusion out of the lobe. The lobe is vertically discretized into a series of discs and the advance of the jet head, expansion of each disc and resulting lobe properties are calculated self-consistently in an iterative manner, also feeding into the particle solver. This method involves a series of assumptions, and various limitations of the method together with possible improvements are discussed in Section 4. We present one single jet model with a flickering jet power and use it to illustrate some general principles relating to the problem of particle acceleration in a variable AGN jet source.

(iii) We find that the synchrotron and UHECR luminosities track the jet power, but with a characteristic response that is determined by the radiative cooling time and UHECR escape time, respectively (Fig. 5). The cooling and escape times act like a low-pass filter on the jet power time series, smoothing out fast variability. The response time changes throughout the jet history, as, typically, the lobe size increases and the magnetic field decreases over time.

(iv) The variable jet power creates a series of electron populations with different normalizations, which are in turn each subjected to a different cooling history. Clear kinks and inflection points are observed in the electron spectrum and resultant SED (Fig. 8). Jet variability therefore produces complexity and curvature in the electron and radiated spectrum that clearly differs from the expected spectrum for constant jet power or for a single electron population.

(v) The CR spectrum inside the lobe follows the spectrum at acceleration, but with a break energy determined by the CR escape time (Fig. 6). This break is smoothed out due to the varying magnetic field and lobe size. For our assumed energy dependence of the diffusion coefficient, the escaping spectrum follows an  $E^{-p+1}$  spectrum up to a cutoff at a maximum CR energy dictated by the jet power.

(vi) The total integrated CR spectrum (the sum of the escaping and internal spectrum) displays a cutoff that is similar to a stretched exponential. In the absence of CR losses, the shape of this exponential

is equal to the expectation value of the cut-off function, such that the differential spectrum obeys (see Section 3.3 and Appendix B)

$$n(E) \propto \int_0^\infty \exp \left[ -\frac{E}{k_E} \sqrt{\frac{1}{Q_j}} \right] Q_j p(Q_j) dQ_j.$$

In situations where the maximum particle energy is determined by the source power, it may be possible to search for evidence of jet variability by studying the cut-off shape. In addition, the cutoff is likely in general to be smoother and more gradual than a pure exponential, and the energy of the cutoff is more reflective of the most powerful outbursts than the mean or median maximum energy.

(vii) We introduce the idea of ‘proxy electrons’ – non-thermal electrons that are cooling at the same rate that UHECRs are escaping from the source (Section 4.1). We use this concept to derive an optimum observing frequency, the frequency of radiation that best tracks the UHECR luminosity. For our assumptions about CR escape, this frequency is typically 20 GHz for a 10  $\mu$ G field, with corresponding inverse Compton emission at  $\sim$ MeV energies. These values suggest radio luminosity may be reasonable UHECR luminosity proxy, but this is strongly dependent on physical parameters in the individual sources as well as the uncertain CR transport physics.

(viii) Some local radio galaxies (such as Cen A and Fornax A) display characteristics of variable jet powers in a morphological sense. These same radio galaxies make for compelling UHECR sources. We discussed parallels with SNRs and propose a scenario somewhat analogous to Galactic CR production, in which the highest energy CRs are accelerated in recent outbursts in local sources, whereas UHECRs around the ankle would come from a near-isotropic background of radio galaxies as discussed by Eichmann (2019a).

Our work highlights the influence of variability in the jet power on particle acceleration in radio galaxies and their resulting spectra and morphologies. It also emphasizes the importance of stochasticity for UHECR source models, particularly for local sources and at the highest energies.

## ACKNOWLEDGEMENTS

We thank the anonymous referee for a thorough, helpful, and constructive report. JM acknowledges a Herchel Smith research fellowship at Cambridge. We gratefully acknowledge the use of the following software packages: ASTROPY (Astropy Collaboration 2013, 2018), MATPLOTLIB 2.0.0 (Hunter 2007), and GAMERA (Hahn 2015). We would like to thank Tony Bell, Katherine Blundell, Sam Connolly, Will Alston, and the attendees of the UK radio-loud AGN meetings for useful discussions.

## DATA AVAILABILITY

The data produced as part of this work are available from the authors on reasonable request.

## REFERENCES

Abdalla H. et al., 2020, *Nature*, 582, 356  
 Abeysekara A. U. et al., 2018, *Nature*, 562, 82  
 Aglietta M. et al., 2004, *Astropart. Phys.*, 20, 641  
 Aharonian F. A., 2000, *New Astron.*, 5, 377  
 Aharonian F. A., 2002, *MNRAS*, 5, 377  
 Alston W. N., 2019, *MNRAS*, 485, 260  
 Alves Batista R. et al., 2016, *J. Cosmol. Astropart. Phys.*, 05, 038

Araudo A. T., Bell A. R., Crilly A., Blundell K. M., 2016, *MNRAS*, 460, 3554  
 Araudo A. T., Bell A. R., Blundell K. M., Matthews J. H., 2018, *MNRAS*, 473, 3500  
 Arnaud M., Pointecouteau E., Pratt G. W., 2005, *A&A*, 441, 893  
 Arnaud M., Pratt G. W., Piffaretti R., B’ohringer H., Croston J. H., Pointecouteau E., 2010, *A&A*, 517, A92  
 Astropy Collaboration, 2013, *A&A*, 558, A33.  
 Astropy Collaboration, 2018, *AJ*, 156, 123.  
 Beckmann R. S. et al., 2019, *A&A*, 631, A60  
 Begelman M. C., Cioffi D. F., 1989, *ApJ*, 345, L21  
 Bell A. R., 1978, *MNRAS*, 182, 147  
 Bell A. R., 2014, *Braz. J. Phys.*, 44, 415  
 Bell A. R., Schure K. M., Reville B., Giacinti G., 2013, *MNRAS*, 431, 415  
 Bell A. R., Araudo A. T., Matthews J. H., Blundell K. M., 2018, *MNRAS*, 473, 2364  
 Bell A. R., Matthews J. H., Blundell K. M., 2019, *MNRAS*, 488, 2466  
 Best P. N., Heckman T. M., 2012, *MNRAS*, 421, 1569  
 Biteau J., Giebels B., 2012, *A&A*, 548, A123  
 Blandford R. D., 2000, *Phys. Scr. T*, 85, 191  
 Blandford R. D., Znajek R. L., 1977, *MNRAS*, 179, 433  
 Blandford R., Meier D., Readhead A., 2019, *ARA&A*, 57, 467  
 Blasi P., 2013, *A&AR*, 21, 70  
 Blasi P., Amato E., 2012a, *J. Cosmol. Astropart. Phys.*, 2012, 010  
 Blasi P., Amato E., 2012b, *J. Cosmol. Astropart. Phys.*, 2012, 011  
 Blundell K. M., Rawlings S., Willott C. J., 1999, *AJ*, 117, 677  
 Bourne M. A., Sijacki D., 2020, preprint ([arXiv:2008.12784](https://arxiv.org/abs/2008.12784))  
 Brienza M. et al., 2018, *A&A*, 618, A45  
 Caprioli D., Blasi P., Amato E., 2011, *Astropart. Phys.*, 34, 447  
 Caprioli D., Yi D. T., Spitkovsky A., 2017, *Phys. Rev. Lett.*, 119, 171101  
 Chang J. S., Cooper G., 1970, *J. Comput. Phys.*, 6, 1  
 Chatterjee K., Liska M., Tchekhovskoy A., Markoff S. B., 2019, *MNRAS*, 490, 2200  
 Chen X., Pohl M., B’ottcher M., Gao S., 2016, *MNRAS*, 458, 3260  
 Chevalier J., Sanchez D. A., Serpico P. D., Lenain J.-P., Maurin G., 2019, *MNRAS*, 484, 749  
 Chiaberge M., Ghisellini G., 1999, *MNRAS*, 306, 551  
 Connolly S. D., 2015, Astrophysics Source Code Library, record ascl:1602.012, preprint ([arXiv:1503.06676](https://arxiv.org/abs/1503.06676))  
 Cooper A. J., Gaggero D., Markoff S., Zhang S., 2020, *MNRAS*, 493, 3212  
 Croston J. H., Birkinshaw M., Hardcastle M. J., Worrall D. M., 2004, *MNRAS*, 353, 879  
 Croston J. H., Hardcastle M. J., Harris D. E., Belsole E., Birkinshaw M., Worrall D. M., 2005, *ApJ*, 626, 733  
 Croston J. H. et al., 2009, *MNRAS*, 395, 1999  
 Croston J. H., Ineson J., Hardcastle M. J., 2018, *MNRAS*, 476, 1614  
 Crusius A., Schlickeiser R., 1986, *A&A*, 164, L16  
 de Souza V., 2017, XXV European Cosmic Ray Symposium XXV, Turin, Sept. 4-9 2016, preprint ([arXiv:1701.06812](https://arxiv.org/abs/1701.06812))  
 Davis S. W., Tchekhovskoy A., 2020, *ARA&A*, 58, 407  
 DeGroot M., Schervish M., 2012, Probability and Statistics. Addison-Wesley, Boston  
 Eichmann B., 2019 J. Phys. Conf. Series, 1181, 012028  
 Eichmann B., 2019b, J. Phys. Conf. Ser., 1181, 012028  
 Eichmann B., Rachen J. P., Merten L., van Vliet A., Becker Tjus J., 2018, *J. Cosmol. Astropart. Phys.*, 2018, 036  
 Eilek J. A., 1996, in Hardee P. E., Bridle A. H., Zensus J. A., eds, ASP Conf. Ser. Vol. 100, Energy Transport in Radio Galaxies and Quasars. Astron. Soc. Pac., San Francisco, p. 281  
 Ellison D. C., Jones F. C., Eichler D., 1981, *J. Geophys.*, 50, 110  
 Emmanoulopoulos D., McHardy I. M., Papadakis I. E., 2013, *MNRAS*, 433, 907  
 Falle S. A. E. G., 1991, *MNRAS*, 250, 581  
 Fender R. P., Belloni T. M., Gallo E., 2004, *MNRAS*, 355, 1105  
 Fender R. P., Maccarone T. J., van Kesteren Z., 2005, *MNRAS*, 360, 1085  
 Finke J. D., Becker P. A., 2014, *ApJ*, 791, 21  
 Fixsen D. J., 2009, *ApJ*, 707, 916

- Fossati G., Maraschi L., Celotti A., Comastri A., Ghisellini G., 1998, *MNRAS*, 299, 433
- Gaskell C. M., 2004, *ApJ*, 612, L21
- Gaspari M., 2016, *Proc. IAU Symp. 319, Galaxies at High Redshift and Their Evolution Over Cosmic Time*. Kluwer, Dordrecht, p. 17
- Ghisellini G., Guilbert P. W., Svensson R., 1988, *ApJ*, 334, L5
- Ghisellini G., Celotti A., Fossati G., Maraschi L., Comastri A., 1998, *MNRAS*, 301, 451
- Gilmore R. C., Somerville R. S., Primack J. R., Domínguez A., 2012, *MNRAS*, 422, 3189
- Globus N., Levinson A., 2016, *MNRAS*, 461, 2605
- Godfrey L. E. H., Shabala S. S., 2013, *ApJ*, 767, 12
- Greisen K., 1966, *Phys. Rev. Lett.*, 16, 748
- Guedes Lang R., Taylor A. M., Ahlers M., de Souza V., 2020, preprint (arXiv:2005.14275)
- H. E. S. S. Collaboration, 2010, *A&A*, 520, A83
- H. E. S. S. Collaboration, 2017, *A&A*, 598, A39
- Hahn J., 2015, 34th International Cosmic Ray Conference (ICRC2015). p. 917
- Hardcastle M. J., 2018, *MNRAS*, 475, 2768
- Hardcastle M. J., Alexander P., Pooley G. G., Riley J. M., 1998, *MNRAS*, 296, 445
- Hardcastle M. J., Cheung C. C., Feain I. J., Stawarz L., 2009, *MNRAS*, 393, 1041
- Harwood J. J., Hardcastle M. J., Croston J. H., Goodger J. L., 2013, *MNRAS*, 435, 3353
- Harwood J. J., Hardcastle M. J., Croston J. H., 2015, *MNRAS*, 454, 3403
- Heil L. M., Vaughan S., Uttley P., 2012, *MNRAS*, 422, 2620
- Heinz S., Sunyaev R., 2002, *A&A*, 390, 751
- Hillas A. M., 1984, *ARA&A*, 22, 425
- Hunter J. D., 2007, *Comput. Sci. Eng.*, 9, 90
- Ineson J., Croston J. H., Hardcastle M. J., Mingo B., 2017, *MNRAS*, 467, 1586
- Iodice E. et al., 2017, *ApJ*, 839, 21
- Iyomoto N., Makishima K., Tashiro M., Inoue S., Kaneda H., Matsumoto Y., Mizuno T., 1998, *ApJ*, 503, L31
- Kaiser C. R., Alexander P., 1997, *MNRAS*, 286, 215
- Kaiser C. R., Schoenmakers A. P., Röttgering H. J. A., 2000, *MNRAS*, 315, 381
- Konar C., Hardcastle M. J., Croston J. H., Jamroz M., Hota A., Das T. K., 2019, *MNRAS*, 486, 3975
- Kotera K., Allard D., Murase K., Aoi J., Dubois Y., Pierog T., Nagataki S., 2009, *ApJ*, 707, 370
- Laing R. A., Jenkins C. R., Wall J. V., Unger S. W., 1994, in Bicknell G. V., Dopita M. A., Quinn P. J., eds, *ASP Conf. Ser. Vol. 54, The Physics of Active Galaxies*. Astron. Soc. Pac., San Francisco, p. 201
- LaMassa S. M. et al., 2015, *ApJ*, 800, 144
- Landau L. D., Lifshitz E. M., 1975, *The Classical Theory of Fields*. Pergamon Press, Oxford
- Lanz L., Jones C., Forman W. R., Ashby M. L. N., Kraft R., Hickox R. C., 2010, *ApJ*, 721, 1702
- Lemoine M., Pelletier G., 2010, *MNRAS*, 402, 321
- Liska M. T. P., Tchekhovskoy A., Quataert E., 2020, *MNRAS*, 494, 3656
- Lovelace R. V. E., 1976, *Nature*, 262, 649
- Maccagni F. M. et al., 2020, *A&A*, 634, A9
- Mackie G., Fabbiano G., 1998, *AJ*, 115, 514
- MacLeod C. L. et al., 2016, *MNRAS*, 458, 389
- Mahatma V. H., Hardcastle M. J., Croston J. H., Harwood J., Ineson J., Moldon J., 2020, *MNRAS*, 491, 5015
- Malzac J., 2014, *MNRAS*, 443, 299
- Malzac J. et al., 2018, *MNRAS*, 480, 2054
- Marcowith A. et al., 2016, *Rep. Prog. Phys.*, 79, 046901
- Marti J. M., Müller E., Font J. A., Ibáñez J. M. Z., Marquina A., 1997, *ApJ*, 479, 151
- Massaglia S., 2007a, *Nucl. Phys. B*, 165, 130
- Massaglia S., 2007b, *Nucl. Phys. B*, 168, 302
- Matthews J. H., Bell A. R., Blundell K. M., Araudo A. T., 2018, *MNRAS*, 479, L76
- Matthews J. H., Bell A. R., Araudo A. T., Blundell K. M., 2019a, in *EPJ Web Conf.*, 210, 04002
- Matthews J. H., Bell A. R., Blundell K. M., Araudo A. T., 2019b, *MNRAS*, 482, 4303
- Matthews J. H., Bell A. R., Blundell K. M., 2020, *New Astron. Rev.*, 89, 101543
- Mignone A., Bodo G., Massaglia S., Matsakos T., Tesileanu O., Zanni C., Ferrari A., 2007, *ApJS*, 170, 228
- Miralda-Escude J., Waxman E., 1996, *ApJ*, 462, L59
- Morganti R., Killeen N. E. B., Ekers R. D., Oosterloo T. A., 1999, *MNRAS*, 307, 750
- Morris P. J., Chakraborty N., Cotter G., 2019, *MNRAS*, 489, 2117
- Narayan R., Igumenshchev I. V., Abramowicz M. A., 2003, *PASJ*, 55, L69
- Neff S. G., Eilek J. A., Owen F. N., 2015, *ApJ*, 802, 88
- Nizamov B. A., Pshirkov M. S., 2020, *J. Cosmol. Astropart. Phys.*, 2020, 060
- Norman C. A., Melrose D. B., Achterberg A., 1995, *ApJ*, 454, 60
- Pfrommer C., Pakmor R., Schaal K., Simpson C. M., Springel V., 2017, *MNRAS*, 465, 4500
- Pierre Auger Collaboration, 2017, *J. Cosmol. Astropart. Phys.*, 2017, 038
- Press W. H., 1978, *Comments Astrophys.*, 7, 103
- Reville B., Bell A. R., 2014, *MNRAS*, 439, 2050
- Reynolds C. S., Heinz S., Begelman M. C., 2002, *MNRAS*, 332, 271
- Richards G. T. et al., 2011, *AJ*, 141, 167
- Runnoe J. C. et al., 2016, *MNRAS*, 455, 1691
- Scaringi S., K'ording E., Uttley P., Knigge C., Groot P. J., Still M., 2012, *MNRAS*, 421, 2854
- Shibata M., Katayose Y., Huang J., Chen D., 2010, *ApJ*, 716, 1076
- Sikora M., Kirk J. G., Begelman M. C., Schneider P., 1987, *ApJ*, 320, L81
- Stickel M., van der Hulst J. M., van Gorkom J. H., Schiminovich D., Carilli C. L., 2004, *A&A*, 415, 95
- Tadhunter C. N., Morganti R., Robinson A., Dickson R., Villar-Martin M., Fosbury R. A. E., 1998, *MNRAS*, 298, 1035
- Taub A. H., 1948, *Phys. Rev.*, 74, 328
- Tchekhovskoy A., Narayan R., McKinney J. C., 2011, *MNRAS*, 418, L79
- Timmer J., Koenig M., 1995, *A&A*, 300, 707
- Turner R. J., 2018, *MNRAS*, 476, 2522
- Turner R. J., Shabala S. S., Krause M. G. H., 2018, *MNRAS*, 474, 3361
- Uttley P., McHardy I. M., 2001, *MNRAS*, 323, L26
- Uttley P., McHardy I. M., Vaughan S., 2005, *MNRAS*, 359, 345
- Vaidya B., Mignone A., Bodo G., Rossi P., Massaglia S., 2018, *ApJ*, 865, 144
- Van de Sande M., Scaringi S., Knigge C., 2015, *MNRAS*, 448, 2430
- Waxman E., 1995, *ApJ*, 452, L1
- Wykes S., Taylor A. M., Bray J. D., Hardcastle M. J., Hillas M., 2018, *Nucl. Part. Phys. Proc.*, 297, 234
- Wykes S. et al., 2019, *MNRAS*, 485, 872
- Yang H.-Y. K., Reynolds C. S., 2016, *ApJ*, 829, 90
- Zatsepin G. T., Kuz'min V. A., 1966, *J. Exp. Theor. Phys. Lett.*, 4, 78

## APPENDIX A: DYNAMIC MODEL FOR THE JET AND LOBE

We consider a light jet propagating in the  $z$  direction into an isothermal ambient medium with a decreasing density and pressure. Our jet model involves the discretization of the  $z$ -domain into a series of disc-shaped cells with height  $\Delta z = 0.01$  kpc. The length of the jet after  $n$  time-steps is then  $L_n = n\Delta z$  where the dynamic time-step  $\Delta t = \Delta z/v_h$  (note that there is a separate time-step for the particle solver, see Section A1 of this appendix). The advance speed  $v_h$  of the jet head is chiefly governed by ram pressure balance, such that  $v_h$  depends on the jet speed and density contrast with the surrounding



medium and is given by (e.g. Marti et al. 1997)

$$v_h = \frac{dz_j}{dt} = \xi \frac{\sqrt{\eta_r^*}}{1 + \sqrt{\eta_r^*}} v_j, \quad (\text{A1})$$

where  $\eta_r^*$  follows the notation of Marti et al. (1997) and represents the relativistic generalization of the density contrast. For non-relativistic internal energies in the jet beam and ambient medium, as assumed here, the specific enthalpy can be neglected and  $\eta_r^* = \Gamma_j^2 \rho_j / \rho_a(z)$ , where  $\rho_a(z)$  is the ambient medium density at distance  $z$ . Note that  $\eta_r^*$  tends to the density ratio  $\rho_j / \rho_a$  as  $\Gamma_j \rightarrow 1$ .  $\xi = 1/4$  is a geometric factor, which we chose to give reasonable advance speeds of  $\approx 0.01c$ . The physical motivation for the factor  $\xi$  is that the jet termination shock has a smaller area than the bow shock, so the pressure acts over a wider area and slows the advance.

Each disc-shaped cell has zero width until the jet material enters it, at which point the width of cell  $i$  is evolved according to  $w_{n+1,i} = w_{n,i} + v_\perp \Delta t$ . This sideways expansion is governed by the expansion speed of the bow shock. If the shocked gas between the bow shock and the contact discontinuity is in pressure equilibrium with the lobe, then, from momentum conservation, we can write

$$v_\perp(\mathbf{r}) = \frac{P - P_a(\mathbf{r})}{\rho_a(\mathbf{r})} \sin \phi, \quad (\text{A2})$$

where  $\phi$  is the angle between the local bow shock normal and the direction of jet propagation and  $\mathbf{r}$  is the position of the edge of the cell. This equation states that the transverse expansion of the lobe is driven by the pressure difference between the lobe and the ambient medium.  $v_\perp$  is a function of position since  $P_a$  and  $\rho$  both decrease away from the origin. The ambient pressure is modelled according to the pressure profile described in Section 2.2. We obtain  $P$  by calculating the internal energy in the lobes and converting to pressure

$$P = \frac{\gamma - 1}{V(t)} \int_0^t \epsilon_w Q_j(t) dt, \quad (\text{A3})$$

where  $\gamma = 4/3$  is the adiabatic index and the volume is obtained by integrating over each cylindrical cell of width  $w$ , that is

$$V(t) = \int_0^{L(t)} 2\pi w(z, t) dz. \quad (\text{A4})$$

This set of equations is evolved numerically as an initial value problem and thus requires an initial condition for the starting lobe geometry – for this purpose, we assume that the base of the lobe initially has a width  $L(t_1)/2$ . The outline of the lobe at 5 Myr intervals is shown in Fig. A1.

### A1 Particle solver and time-stepping

The particle solver operates inside the main dynamic loop and undergoes a series of subcycles per dynamic time-step. The time-step is calculated as

$$\Delta t|_p = C_f \frac{N_m}{dN_m/dt} \Big|_{\min, \text{allm}}, \quad (\text{A5})$$

where  $C_f = 0.4$  is a Courant-type number and  $m$  is an index denoting the energy bin, and we only include bins with  $N_m > 10^{-15} N_{m,\text{max}}$  so as to avoid small time-steps from fast-cooling bins with negligible numbers of particles. The TDMA solver and synchrotron emissivity calculation form part of a PYTHON package called MSYNCHRO. We have tested the TDMA code using single injections of power law and delta function electron distributions and comparing to analytical formulae. We have also tested the synchrotron code against the

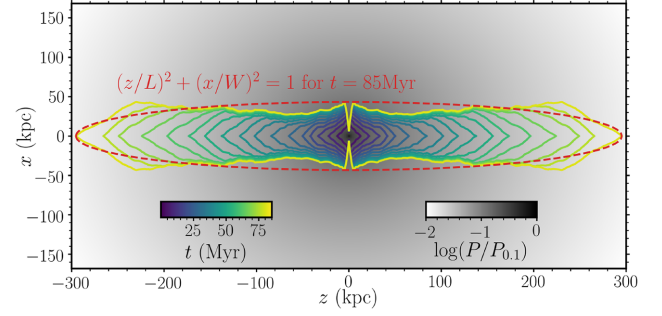


**Figure A1.** The evolution of the jet lobe in the reference model over time. The coloured lines show the outline of the lobe at 5 Myr intervals, with the colour scale matching that in Fig. 8. The red line shows the outline of the ellipse used to calculate the escape time in equation (13) near the end of the source evolution at  $t = 85$  Myr. The background colour shows the pressure of the surrounding environment, normalized to the pressure at 0.1 kpc from the centre ( $P_{0.1} = 76.3 \text{ eV cm}^{-3}$ ).

SYNCH code from Hardcastle et al. (1998) and the GAMERA code (Hahn 2015). The tests result in extremely close agreement and are documented within the MSYNCHRO code repository.<sup>1</sup>

## APPENDIX B: THE SHAPE OF THE CUTOFF IN THE COSMIC RAY SPECTRUM

The variation in jet power causes a corresponding variation in the maximum CR energy. The maximum CR energy is given by equation (11), and can be written more simply as  $E_{\text{max},i} = k_E \sqrt{Q_j / \beta_j}$  where  $k_E = \eta_H Z_i \sqrt{\epsilon_b}$ . The variation in maximum energy means that the source term has a cut-off function that varies over time, with a corresponding effect on the overall spectrum. To illustrate this, we consider the continuity equation (9) governing the evolution of CR ions. We focus on one CR species (protons) and ignore both the cooling and escape loss terms, such that  $dn_i(E)/dt = S(E/Z_i, f_i, t)$ . The source term  $S(E/Z_i, f_i, t)$  is given by equation (10), and, if we neglect the (weak) variation in the  $\ln(E_{\text{max}}/E_0)$  term, we can write it as

$$S(E/Z_i, f_i, t) \propto Q_j(t) E^{-p} e^{-E/E_{\text{max},i}}. \quad (\text{B1})$$

We can integrate  $dn_i(E)/dt$  so that, after a time interval  $\Delta t$  the spectrum is

$$n_i(E) \propto E^{-p} \int_0^{\Delta t} Q_j(t) \exp \left[ -\frac{E}{k_E \sqrt{Q_j(t)}} \right] dt. \quad (\text{B2})$$

If we take the limit of large  $\Delta t$ , we can make use of the ‘law of the unconscious statistician’ (e.g. DeGroot & Schervish 2012), which states that the expected value of a function  $g(\mathcal{Z})$ , where  $\mathcal{Z}$  is a continuous random variable with PDF  $p(\mathcal{Z})$ , is given by the integral of  $p(\mathcal{Z})g(\mathcal{Z})$  over all  $\mathcal{Z}$ . Thus, if we set  $\beta_j = 1$  for simplicity, the spectrum obeys the proportionality

$$n_i(E) \propto \int_0^\infty p(Q_j) Q_j \exp \left( -\frac{E}{k_E \sqrt{Q_j}} \right) dQ_j, \quad (\text{B3})$$

as given in Section 3.3, and where the positive integration domain reflects the fact that  $Q_j$  cannot be negative. We now focus on the

<sup>1</sup>The MSYNCHRO code is publicly available at <https://github.com/jhmatthews/msynchro>



specific case of our adopted lognormal form for  $p(Q_j)$ , which gives

$$n_i(E) \propto \int_0^\infty \exp \left[ -\frac{E}{k_E} \sqrt{\frac{1}{Q_j}} - \frac{(\ln(Q_j/Q_0))^2}{2\sigma^2} \right] dQ_j. \quad (\text{B4})$$

If we make a change of variables, defining  $x = E/k_E$  and  $y = Q_j/Q_0$ , we can represent the integral in the form

$$f(x, Q_0, \sigma) = \int_{-\infty}^\infty y \exp \left[ -\frac{x}{\sqrt{y}Q_0} - \frac{(\ln y)^2}{2\sigma^2} \right] d \ln y, \quad (\text{B5})$$

where  $f(x, Q_0, \sigma)$  represents the integral in the previous expression, such that  $n_i(E) \propto f(x, Q_0, \sigma)$ . We approximate the integral over  $\ln y$

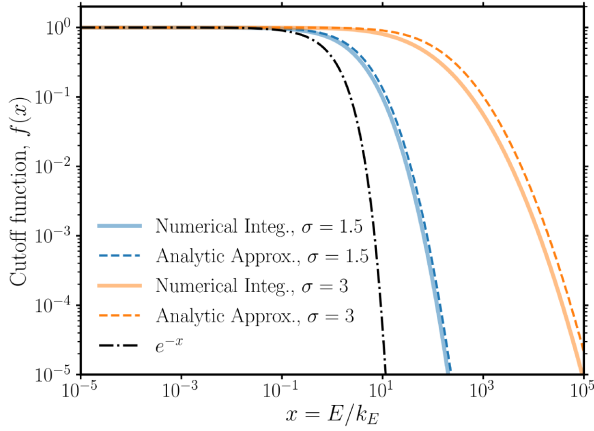


**Figure B1.** A comparison of the approximation to the cut-off function,  $f(x)$  (equation B7), to a numerical integral of equation (B5), for two values of  $\sigma$ . In both cases, we set  $Q_0 = 1$ . We also show a pure exponential on the same plot, showing that more variable sources create cutoffs that are more ‘stretched out’, and with a higher characteristic maximum energy (see also Section 3.3) than for a steady source with  $Q_j = Q_0$ .

by assuming it is dominated by the peak of the integrand term. The peak in the integrand occurs at  $x = 2y_p^{1/2}(\ln y_p/\sigma^2 - 1)$ . Inverting this relation gives

$$y_p(x, \sigma) = \left( \frac{\sigma^2 x/4}{W(e^{-\sigma^2/2} \sigma^2 x/4)} \right)^2, \quad (\text{B6})$$

where  $W(z)$  is the Lambert W-function, which satisfies the relation  $W(z)\exp[W(z)] = z$ . Adopting this integrand peak  $y$ -value,  $y_p$ , the functional form for the cutoff is found,

$$f(x, Q_0, \sigma) \approx y_p \exp \left[ -\frac{x}{\sqrt{Q_0 y_p}} - \frac{(\ln y_p)^2}{2\sigma^2} \right]. \quad (\text{B7})$$

This description is found to accurately characterize the cut-off shape, over 10 decades in  $f$  and for a range of values of  $\sigma$ . To illustrate this, we show a comparison between the analytical approximation (equation B7) with a numerical solution to equation (B5) in Fig. B1, for two values of  $\sigma$ .

This paper has been typeset from a  $\text{\LaTeX}$  file prepared by the author.